

USER GUIDE
Planetary-Code-Collection:
Thermal and Ice Evolution Models
for Planetary Surfaces

Norbert Schörghofer (norbert@psi.edu)
Honolulu, Hawaii

2002–2022
Last updated January 24, 2022

Contents

1	Conduction of Heat: 1D Thermal Model for Planetary Surfaces	4
1.1	Semi-Implicit Scheme on Irregular Grid	4
1.1.1	Upper boundary condition: Stefan-Boltzmann radiation law	5
1.1.2	Upper boundary condition: prescribed T	6
1.1.3	Lower boundary condition	6
1.1.4	Validations	7
1.2	Other Model Components	9
1.2.1	Seasonal frost cover (Mars)	9
1.2.2	Influence of ice on thermal properties	9
1.2.3	Mars atmosphere	10
1.3	Semi-Implicit Scheme for Spherically Symmetric Geometry	11
	Bibliography	13
2	Diffusion of Water Vapor with Phase Transitions	15
2.1	Governing Equations	15
2.2	Discretizations	16
2.2.1	Possible discretizations of spatial derivatives	16
2.2.2	Discretization of time derivative	17
2.2.3	Complete scheme	18
2.2.4	Upper boundary condition	18
2.2.5	Lower boundary condition	19
2.3	Discussion	19
2.3.1	Numerical stability	19
2.3.2	Diffusion-advection	19
	Bibliography	19
3	Long-Term Ice Evolution	20
3.1	Equilibrium Models of Near-Surface Ice on Mars	20
3.2	Asynchronous Model for Ice on Mars	21
3.3	Asynchronous Model for Temperature, Impact Mixing, and Ice Loss on Asteroids	21
3.4	Lunar Thermal Ice Pump	21
	Bibliography	22

4	Terrestrial Analogs	24
4.1	Mauna Kea atmosphere	24
4.2	Dry Valleys of Antarctica	25
	Bibliography	25
5	3D Surface Energy Balance	27
5.1	Incidence Angle on Slope	27
5.2	Thermal Model for Tilted Planar Slope	28
5.3	Horizons and Multigrids (Terrain Shadowing)	29
5.4	Governing Equations with Terrain Irradiance	30
5.5	View Factors	31
5.6	Diffuse Sky Irradiance in the Presence of Horizons	34
5.7	Outline of Implementation	35
	Bibliography	36
6	Surface-bounded Exospheres	38
6.1	Introduction	38
6.2	Ballistic Flight on Sphere	38
	6.2.1 Constant gravity	39
	6.2.2 Non-uniform gravity	39
	6.2.3 Coriolis effect	40
6.3	Other Model Components	41
	6.3.1 Initial velocities	41
	6.3.2 Photo-destruction	41
	6.3.3 Event driver	41
	6.3.4 Residence times	42
	Bibliography	42

Preface

Companion to <https://github.com/nschorgh/Planetary-Code-Collection/>

Cite user guide or source code as:

N. Schörghofer. Planetary-Code-Collection: Thermal and Ice Evolution Models for Planetary Surfaces, 2021. GitHub. doi:10.5281/zenodo.594268 <https://github.com/nschorgh/Planetary-Code-Collection/>

The most recent release is usually behind the most recent version available on GitHub, but releases have DOIs that can be cited.

Releases are available from GitHub and Zendodo. Each release has a version number and a dedicated DOI, whereas the above DOI refers to all versions, past and future. Individual DOIs are listed at <https://zenodo.org/record/594268>

Technical Notes:

Most of the code was developed with a `gfortran` compiler on an Intel processor. Many components were also run on various Linux clusters, sometimes using other compilers. The non-portable `real(8)` and `real*8` are meant to correspond to an 8-byte floating point number.

Part 1

Conduction of Heat: 1D Thermal Model for Planetary Surfaces

1-Dimensional Numerical Model of Thermal Conduction and Surface Energy Balance

Authors & History: originally implemented by Samar Khatiwala in 2001 (including upper radiation boundary condition for semi-implicit scheme); extended to variable thermal properties and irregular grid by Norbert Schörghofer 2002–2003; added predictor-corrector step in 2019

Governing equation for the surface energy balance:

$$\rho c \frac{\partial T}{\partial t} = \frac{\partial}{\partial z} \left(k \frac{\partial T}{\partial z} \right) \quad (1.1)$$

T ... temperature, t ... time, z ... depth, ρc ... volumetric heat capacity, k ... thermal conductivity

$F = k \frac{\partial T}{\partial z}$... heat flux

+ various boundary conditions specified below. Note that a radiation upper boundary condition is non-linear, and needs to be linearized for an implicit numerical solver.

1.1 Semi-Implicit Scheme on Irregular Grid

$$\frac{\partial}{\partial z} F_j = \frac{F_{j+\frac{1}{2}} - F_{j-\frac{1}{2}}}{(z_{j+1} - z_{j-1})/2} = 2 \frac{k_{j+\frac{1}{2}} \frac{T_{j+1} - T_j}{z_{j+1} - z_j} - k_{j-\frac{1}{2}} \frac{T_j - T_{j-1}}{z_j - z_{j-1}}}{z_{j+1} - z_{j-1}}$$

$$\begin{aligned} (\rho c)_j \frac{\partial T_j}{\partial t} = & \frac{2k_{j+\frac{1}{2}}}{(z_{j+1} - z_j)(z_{j+1} - z_{j-1})} T_{j+1} - \frac{2}{z_{j+1} - z_{j-1}} \left(\frac{k_{j+\frac{1}{2}}}{z_{j+1} - z_j} + \frac{k_{j-\frac{1}{2}}}{z_j - z_{j-1}} \right) T_j + \\ & + \frac{2k_{j-\frac{1}{2}}}{(z_j - z_{j-1})(z_{j+1} - z_{j-1})} T_{j-1} \end{aligned}$$

$$\text{introduce } \alpha_j = \frac{\Delta t}{(\rho c)_j} \frac{k_{j+\frac{1}{2}}}{(z_{j+1} - z_j)(z_{j+1} - z_{j-1})} \quad \text{and} \quad \gamma_j = \frac{\Delta t}{(\rho c)_j} \frac{k_{j-\frac{1}{2}}}{(z_j - z_{j-1})(z_{j+1} - z_{j-1})} \quad (1.2)$$

$$\begin{aligned}
\Delta t \frac{\partial T_j}{\partial t} &= 2\alpha_j T_{j+1} - 2(\alpha_j + \gamma_j) T_j + 2\gamma_j T_{j-1} \\
T_j^{n+1} - T_j^n &= \alpha_j T_{j+1}^{n+1} - (\alpha_j + \gamma_j) T_j^{n+1} + \gamma_j T_{j-1}^{n+1} + \alpha_j T_{j+1}^n - (\alpha_j + \gamma_j) T_j^n + \gamma_j T_{j-1}^n \\
\boxed{-\alpha_j T_{j+1}^{n+1} + (1 + \alpha_j + \gamma_j) T_j^{n+1} - \gamma_j T_{j-1}^{n+1} &= \alpha_j T_{j+1}^n + (1 - \alpha_j - \gamma_j) T_j^n + \gamma_j T_{j-1}^n} \quad 1 < j < N
\end{aligned} \tag{1.3}$$

Superscript n refers to the time step. Subscript j refers to position z_j . Whereas the temperature T_j is defined on grid point z_j , the conductivity k is defined on half-points. In the equations above, $(\rho c)_j$ is defined on z_j , but in the program implementations, $2(\rho c)_j = (\rho c)_{j+\frac{1}{2}} + (\rho c)_{j-\frac{1}{2}}$. In this way, the thermal properties k and ρc are defined on the same points. And they do not need to be defined at an interface of two layers with different thermal properties when that interface coincides with a grid point. Since array indices must be integers, we choose $k[j] = k_{j-\frac{1}{2}}$, and the same for ρc .

1.1.1 Upper boundary condition: Stefan-Boltzmann radiation law

$$Q + k \left. \frac{\partial T}{\partial z} \right|_{z=0} = \epsilon \sigma T^4 \Big|_{z=0} \tag{1.4}$$

Q is the incoming solar flux including the atmospheric contribution.

introduce auxiliary quantity T_0 , such that surface temperature $T_s = (T_0 + T_1)/2$

$$\left. \frac{\partial T}{\partial z} \right|_{z=0} = \frac{T_1 - T_0}{\Delta z} \quad \text{and} \quad T^4 \Big|_{z=0} = \left(\frac{T_0 + T_1}{2} \right)^4 \quad \text{with} \quad \Delta z = 2z_1$$

$T = T_r + T'$ T_r is a reference temperature around which we linearize

$$\begin{aligned}
Q + k_{1/2} \frac{T_1 - T_0}{\Delta z} &= \epsilon \sigma \left(\frac{2T_r + T'_0 + T'_1}{2} \right)^4 \\
&\approx \epsilon \sigma T_r^4 + 2\epsilon \sigma T_r^3 (T'_0 + T'_1) \\
&= -3\epsilon \sigma T_r^4 + 2\epsilon \sigma T_r^3 (T_0 + T_1)
\end{aligned}$$

$$T_0 \left(\frac{k_{1/2}}{\Delta z} + B(T_r) \right) = Q + 3\epsilon \sigma T_r^4 + T_1 \left(\frac{k_{1/2}}{\Delta z} - B(T_r) \right) \quad \text{where} \quad B(T_r) = 2\epsilon \sigma T_r^3$$

introduce $a = (Q + 3\epsilon \sigma T_r^4) / \left(\frac{k}{\Delta z} + B \right)$ and $b = \left(\frac{k_{1/2}}{\Delta z} - B \right) / \left(\frac{k_{1/2}}{\Delta z} + B \right)$

The relation for $j = 1$ is then

$$-\alpha_1 T_2^{n+1} + (1 + \alpha_1 + \gamma_1 - \gamma_1 b^{n+1}) T_1^{n+1} = \alpha_1 T_2^n + (1 - \alpha_1 - \gamma_1 + \gamma_1 b^n) T_1^n + \gamma_1 (a^n + a^{n+1}) \tag{1.5}$$

define $\beta = \frac{\Delta t}{(\rho c)_1} \frac{1}{2\Delta z^2}$, then $\alpha_1 = \beta k_{3/2}$ and $\gamma_1 = \beta k_{1/2}$

$$\text{surface temperature} \quad T_s = \frac{1}{2}(T_0 + T_1) = \frac{1}{2}(a + bT_1 + T_1)$$

choose $T_r^n = T_s^n$

implemented in `conductionQ.f90`. Note that the uppermost layer is a half-layer, and the

first few grid points must be chosen as $z_0 = 0$ and $z_2 = 3z_1$ (in other words $z_1 = \Delta z/2$, $z_2 = z_1 + \Delta z$). The coefficients for the nonlinear upper boundary condition are designed for that. Subroutine `setgrid` can be used to generate an appropriate grid.

Modified treatment of the upper boundary helpful in some situations: The linearization of the Stefan-Boltzmann law, σT^4 , works well as long as the surface temperature changes slowly. The above approximation works very well for most situations, such as Mars orbit and a horizontal surface. A temporary instability, where the surface temperature overshoots significantly, was encountered in two situations: i) A sloped, shadowed surface emerges into sunlight. In this case the energy input changes abruptly. ii) For asteroid orbits with high eccentricity and very small perihelion distances, when the pole emerges from winter into sunlight near perihelion. This transition is continuous, but the change in input energy is nevertheless dramatic.

Above, the thermal emission is linearized around the reference temperature $T_r^n = T_s^n$. If T_s^{n+1} is far from T_s^n , a significant error was incurred in the evaluation of the emitted energy. This can be addressed by repeating the calculation with a new reference temperature T_r somewhere in between T_s^n and T_s^{n+1} . An empirical choice is the geometric mean between the previous reference temperature and the new surface temperature. This method is essentially a predictor-corrector step, iteratively applied until T_r is within 20% of $T_s^{(n+1)}$. It seems this iterative method always converges.

Another approach is “artificial flux smoothing” where the time step is subdivided into many substeps, using linear interpolation of the incoming flux from Q^n to Q^{n+1} . It turns a discontinuous change in Q into a continuous change. However, this does not answer how a nascent instability is identified or how many substeps are required to cure it.

1.1.2 Upper boundary condition: prescribed T

standard formulas (1.2,1.3) with $T_0 = T_s$ and $z_0 = 0$

$$\alpha_1 = \frac{\Delta t}{(\rho c)_1} \frac{k_{3/2}}{(z_2 - z_1)z_2}, \quad \gamma_1 = \frac{\Delta t}{(\rho c)_1} \frac{k_{1/2}}{z_1 z_2}$$

$$-\alpha_1 T_2^{n+1} + (1 + \alpha_1 + \gamma_1) T_1^{n+1} = \alpha_1 T_2^n + (1 - \alpha_1 - \gamma_1) T_1^n + \gamma_1 (T_s^n + T_s^{n+1})$$

implemented in `conductionT.f90`

1.1.3 Lower boundary condition

(assume $z_{N+1} - z_N = z_N - z_{N-1} =: \Delta z$)

No heat flux: $F_{N+\frac{1}{2}} = 0 \Rightarrow k_{N+\frac{1}{2}}(T_{N+1} - T_N) = 0 \Rightarrow T_{N+1} = T_N$

$$(1 + \gamma_N) T_N^{n+1} - \gamma_N T_{N-1}^{n+1} = (1 - \gamma_N) T_N^n + \gamma_N T_{N-1}^n$$

$$\gamma_N = \frac{\Delta t}{(\rho c)_N} \frac{k_{N-\frac{1}{2}}}{2(z_N - z_{N-1})^2}$$

Or geothermal heating: $F_{N+\frac{1}{2}} = F_{\text{geothermal}} \Rightarrow k_{N+\frac{1}{2}}(T_{N+1} - T_N) = \Delta z F_{\text{geothermal}}$

$$(1 + \gamma_N)T_N^{n+1} - \gamma_N T_{N-1}^{n+1} = (1 - \gamma_N)T_N^n + \gamma_N T_{N-1}^n + \frac{\Delta t}{(\rho c)_N} \frac{F_{\text{geothermal}}}{\Delta z}$$

1.1.4 Validations

The following tests were performed for these solvers:

a) For a sinusoidally varying surface temperature, the solution to the heat equation is known analytically:

$$T = T_m + T_a e^{-z/\delta} \sin\left(\frac{z}{\delta} - \frac{2\pi t}{P}\right) \quad (1.6)$$

where

$$\delta = \frac{\Gamma}{\rho c} \sqrt{\frac{P}{\pi}} \quad (1.7)$$

is the thermal skin depth, Γ the thermal inertia, and P the period. This expression can be used to validate `conductionT` for uniform thermal properties (Figure 1.1). The heat flux is given by

$$F = -k \frac{\partial T}{\partial z} = -\sqrt{2} k \frac{T_a}{\delta} e^{-z/\delta} \cos\left(\frac{z}{\delta} - \frac{2\pi t}{P} + \frac{\pi}{4}\right)$$

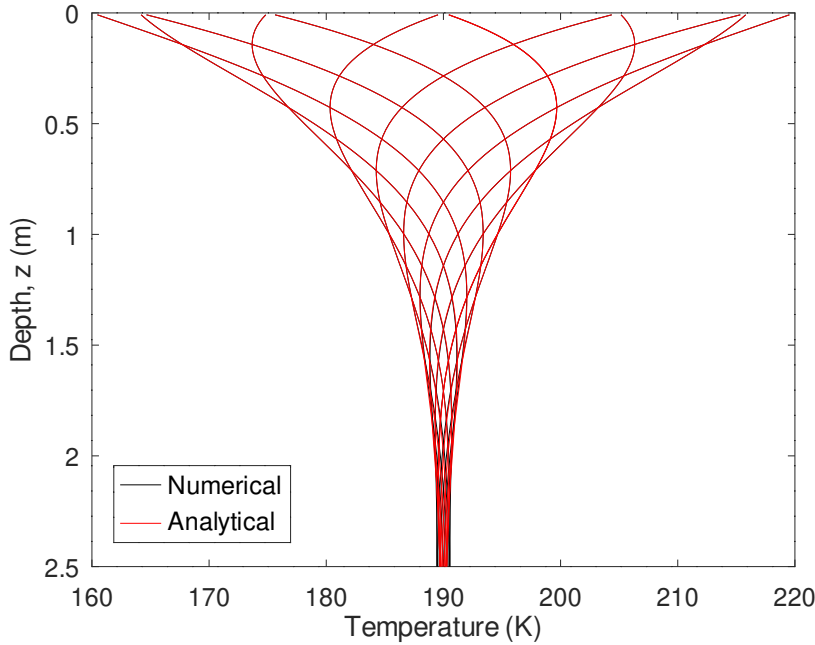


Figure 1.1: Comparison of numerical with analytical solution for Crank-Nicolson solver with periodic surface boundary condition. The deviations at the bottom are justified because the analytical solution (1.6) is for an infinitely deep domain. Non-equidistant grid points were used in this example.

b) Convergence of some solutions with Δt and Δz has been verified.

c) For periodic solutions (of `conductionT` and `conductionQ`) the heat flux $F = -k\partial T/\partial z$, time-averaged over one period, must be the same at all depths and equal to the heat flux imposed at the bottom boundary, even for spatially-varying thermal properties, as long as the heat capacity does not vary with time; consider the time average of eq. (1.1). Figure 1.2 shows one example.

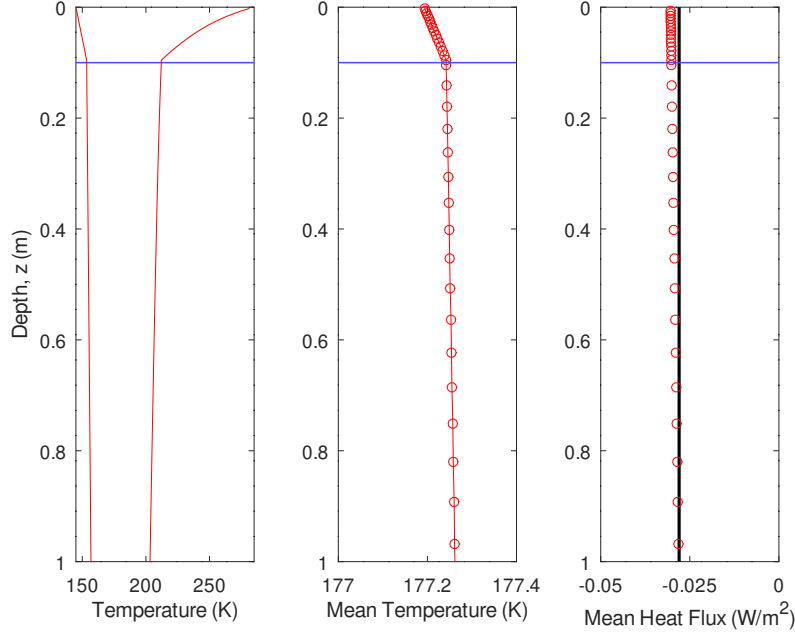


Figure 1.2: Validation of the conservation of the heat flux (flux-conservative discretization). The ice table at 10 cm depth causes dramatic changes in thermal properties. Left panel: Minimum and maximum subsurface temperatures over one Mars year. Middle panel: Temperatures averaged over one Mars year, which change linearly as the thermal conductivity is constant within each of the two layers. Right panel: Heat flux averaged over one Mars year, which is preserved across changes in thermal properties and equals to the heat flux imposed at the bottom boundary of 0.028 W/m^2 .

d) A short-term solution for the heat equation with Stefan-Boltzmann radiation surface boundary condition was derived by Handelsman and Olmstead (1972). Their non-dimensional equations are $T_t = T_{zz}$, $T_z(0, t) = T^n(0, t) - f(t)$, $T(z, 0) = 0$, $\lim_{z \rightarrow \infty} T(z, t) = 0$. In our case $n = 4$ and $f(t) = T_e^4$, where T_e is an ambient temperature. In this case, their solution is $T(0, t) = \frac{2}{\sqrt{\pi}} T_e^4 \sqrt{t}$, for small t . After re-dimensionalizing, the surface temperature is found to change as

$$T(0, t) = T_0 + \frac{2}{\sqrt{\pi}} \frac{\epsilon \sigma}{\Gamma} (T_e^4 - T_0^4) \sqrt{t} \quad \text{for small } t \geq 0 \quad (1.8)$$

where $T_0 = T(0, 0)$ is the initial surface temperature. Figure 1.3 shows that the numerical solver reproduces the expected behavior for this discontinuous change in incoming flux.

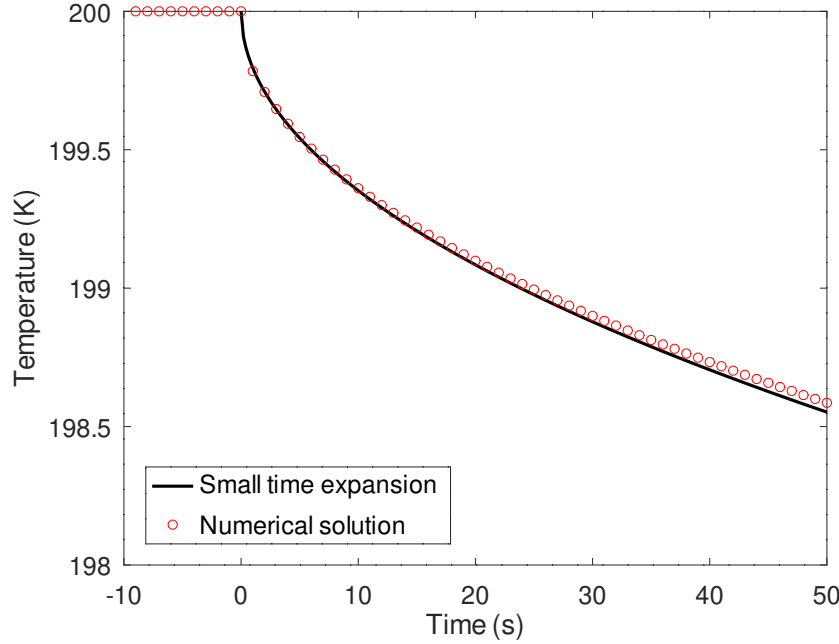


Figure 1.3: Response of numerical solution to a sudden change in incoming flux compared to the analytically obtained expansion for small times, eq. (1.8).

e) When applied to Mars, modeled surface temperatures have been compared to TES (Thermal Emission Spectrometer) surface temperatures.

1.2 Other Model Components

1.2.1 Seasonal frost cover (Mars)

Add latent heat of CO₂ sublimation

$$Q + k \left. \frac{\partial T}{\partial z} \right|_{z=0} = \epsilon \sigma T^4 \Big|_{z=0} + L \frac{dm_{\text{CO}_2}}{dt} \quad (1.9)$$

call `conductionQ` if T_s is above CO₂ frost point or if $m_{\text{CO}_2} = 0$; call `conductionT` if T_s is below CO₂ frost point or if $m_{\text{CO}_2} > 0$; calculate energy difference and add CO₂ mass; adjust surface albedo; repeat this at every time step

1.2.2 Influence of ice on thermal properties

This is only one possible parametrization. In retrospective, it agrees well with the laboratory measurements by Siegler et al. (2012) for vapor-deposited ice.

$$\begin{aligned} \rho c &= (1 - \epsilon) \rho_{\text{regolith}} c_{\text{regolith}} + \epsilon f \rho_{\text{ice}} c_{\text{ice}} \\ k &= (1 - \epsilon) k_{\text{regolith}} + \epsilon f k_{\text{ice}} + (1 - f) \epsilon k_{\text{air}} \end{aligned}$$

ρ ... density; c ... heat capacity; k ... thermal conductivity
 ϵ ... porosity (void space / total volume)
 f ... ice filling fraction ($f = \rho_f / \rho_{\text{ice}}$, ρ_f = density of free ice)

at around 200 Kelvin: $c_{\text{ice}} \approx 1540 \text{ J/(kg K)}$, $\rho_{\text{ice}} \approx 927 \text{ kg/m}^3$, $k_{\text{ice}} \approx 3.2 \text{ W/(m K)}$
 See Winter and Saari (1969) for heat capacity of silicates as a function of temperature.
 See Handbook of Chemistry and Physics (Lide, 2003) for temperature dependence for ice.

In the program, k and ρc are defined halfway between grid points, whereas ρ_f and T are defined on grid points.

1.2.3 Mars atmosphere

The elevation β of the sun above an horizontal horizon is given in terms of geographic latitude λ , declination δ of the sun, and the hour angle h :

$$\sin \beta = \cos \lambda \cos \delta \cos h + \sin \lambda \sin \delta. \quad (1.10)$$

The direct solar insolation is

$$Q_{\text{solar}} = \frac{S_0}{R^2} (1 - A)(1 - f)^{1/\max(\sin \beta, 0.04)} \sin \beta, \quad (1.11)$$

where S_0 is the solar constant, R the distance from the sun in AU, A the albedo, and f due to the extinction in the atmosphere. The length of the path through the atmosphere is proportional to $1/\sin \beta$ and the transmission is taken to be exponential in this path length. The nadir optical depth of the atmosphere is $-\ln(1 - f) \approx f$. For small extinction and away from the horizon, $(1 - f)^{1/\sin \beta} \approx 1 - f/\sin \beta$. The maximum atmospheric path length ℓ_{max} is limited due to the curvature of the planet, $H/\ell_{\text{max}} \approx \sqrt{H/2R} \approx 0.04$ for Mars, where H is the scale height of the atmosphere and R the radius of the planet.

Atmospheric emission is approximated by a fraction f_{IR} (typically 2–4%) of noontime insolation and is kept constant throughout a solar day (Kieffer et al., 1977):

$$Q_{\text{a,IR}} = f_{\text{IR}} \frac{S_0}{R^2} \sin \beta_{\text{noon}} \quad (\text{all day}) \quad (1.12)$$

This approximation fails in the polar regions; in this case, Kieffer et al. (1977) replaces the noontime insolation with the surface frost emission.

In addition, there is scattered light when $\sin \beta > 0$, which is approximated by

$$Q_{\text{a,scat}} = \frac{1}{2} f_{\text{scat}} \frac{S_0}{R^2}. \quad (1.13)$$

Half of the scattered light is assumed to be lost to space.

For the purpose of discussion, we determine the total energy budget of the atmosphere for a horizontal land mass. To first order $(1 - f)^{1/\sin \beta} \sin \beta \approx \sin \beta - f$, in eq. (1.11), so at any time the sun is above the horizon the energy absorbed and scattered in the atmosphere is approximately $(S_0/R^2)f$. Over a solar day

$$\frac{S_0}{R^2} f \int_{\text{daytime}} dh \approx \frac{S_0}{R^2} \pi f. \quad (1.14)$$

The infrared emission from the atmosphere over the same time period is

$$2\pi f_{\text{IR}} \frac{S_0}{R^2} \sin \beta_{\text{noon}} \quad (1.15)$$

and the scattered energy

$$\pi f_{\text{scat}} \frac{S_0}{R^2}. \quad (1.16)$$

The globally averaged $\sin \beta_{\text{noon}}$ is

$$\frac{1}{\pi} \int_{-\pi/2}^{\pi/2} d\lambda \cos \lambda \sin \beta_{\text{noon}} \approx \frac{1}{\pi} \int_{-\pi/2}^{\pi/2} d\lambda \cos^2 \lambda = \frac{1}{2} \quad (1.17)$$

Global balance, (1.14)=(1.15)+(1.16), is achieved with

$$f = f_{\text{IR}} + f_{\text{scat}}.$$

This relation does not hold at an individual latitude, but it does hold globally.

The Mars thermal model was used in Schorghofer and Aharonson (2005) and many subsequent papers, including Schorghofer (2008).

1.3 Semi-Implicit Scheme for Spherically Symmetric Geometry

History: developed 2018–2019

Governing equation (1.1) is appropriate for depths small compared to the radius of the body. In the context of small asteroids, it may be necessary to include the curvature effect. A one-dimensional spherically-symmetric semi-implicit heat solver has been implemented (subroutine `conductionT_sphere` in `sphere1d_implicit.f90`). Conceptually, the derivation is the same as in section 1.1. The implementation is limited to constant grid spacing, uniform thermal properties, and a temperature boundary condition on the surface.

The equation for energy conservation in three dimensions is

$$\rho c \frac{\partial T}{\partial t} - \vec{\nabla} \cdot (k \vec{\nabla} T) = 0 \quad (1.18)$$

In the spherically symmetric (1D) case, this equation becomes

$$\rho c \frac{\partial T}{\partial t} = \frac{1}{r^2} \frac{\partial}{\partial r} \left(k r^2 \frac{\partial T}{\partial r} \right)$$

For spatially uniform k , this simplifies to

$$\frac{\partial T}{\partial t} = \frac{\kappa}{r^2} \frac{\partial}{\partial r} \left(r^2 \frac{\partial T}{\partial r} \right) \quad (1.19)$$

where $\kappa = k/(\rho c)$ is the thermal diffusivity.

The upper (surface) boundary condition is prescribed as a time-dependent temperature $T_0(t)$, which may in turn be obtained from a separate model based on the orbital and physical parameters of the body. At the center of the body $\partial T/\partial r = 0$, which forms the lower boundary condition.

To achieve a spatial discretization that conserves the heat flux, center differences are applied to the equation in the form of (1.19). It would be a mistake to apply the chain rule of differentiation and then discretize. The term in the parenthesis is

$$\left(r^2 \frac{\partial T}{\partial r}\right)_j = r_j^2 \frac{T_{j+1/2} - T_{j-1/2}}{\Delta r}$$

The discretization of the right-hand side of equation (1.19) is:

$$(\text{rhs})_j = \frac{\kappa}{r_j^2 (\Delta r)^2} [r_{j+1/2}^2 T_{j+1} - (r_{j+1/2}^2 + r_{j-1/2}^2) T_j + r_{j-1/2}^2 T_{j-1}]$$

Introduce $c_{j+1/2} = (r_{j+1/2}/r_j)^2$, $c_{j-1/2} = (r_{j-1/2}/r_j)^2$, and $c_j = (c_{j+1/2} + c_{j-1/2})/2$, then this abbreviates to

$$(\text{rhs})_j = \frac{\kappa}{(\Delta r)^2} [c_{j+1/2} T_{j+1} - 2c_j T_j + c_{j-1/2} T_{j-1}]$$

For an explicit scheme

$$\frac{T_j^{n+1} - T_j^n}{\Delta t} = (\text{rhs})_j^n$$

where the superscripts enumerate time steps. For a semi-implicit (Crank-Nicolson) scheme

$$\frac{T_j^{n+1} - T_j^n}{\Delta t} = \frac{1}{2}(\text{rhs})_j^n + \frac{1}{2}(\text{rhs})_j^{n+1} \quad (1.20)$$

It is useful to introduce the abbreviation

$$\alpha = \kappa \frac{\Delta t}{(\Delta r)^2}$$

For the semi-implicit scheme (1.20),

$$T_j^{n+1} - \frac{\alpha}{2} [c_{j+1/2} T_{j+1}^{n+1} - 2c_j T_j^{n+1} + c_{j-1/2} T_{j-1}^{n+1}] = T_j^n + \frac{\alpha}{2} [c_{j+1/2} T_{j+1}^n - 2c_j T_j^n + c_{j-1/2} T_{j-1}^n]$$

From this results the linear system of equations

$$-\frac{\alpha}{2} c_{j+1/2} T_{j+1}^{n+1} + (1 + \alpha c_j) T_j^{n+1} - \frac{\alpha}{2} c_{j-1/2} T_{j-1}^{n+1} = +\frac{\alpha}{2} c_{j+1/2} T_{j+1}^n + (1 - \alpha c_j) T_j^n + \frac{\alpha}{2} c_{j-1/2} T_{j-1}^n \quad (1.21)$$

which is solved numerically by tridiagonal inversion.

At the upper boundary, the temperature T_0 is prescribed. For $j = 1$, equation (1.21) becomes

$$-\frac{\alpha}{2} c_{3/2} T_2^{n+1} + (1 + \alpha c_1) T_1^{n+1} = +\frac{\alpha}{2} c_{3/2} T_2^n + (1 - \alpha c_1) T_1^n + \frac{\alpha}{2} c_{1/2} (T_0^n + T_0^{n+1}) \quad (1.22)$$

For the lower boundary condition, at the center of the sphere ($j = N$): $\partial T/\partial r = 0$ and therefore $T_{N+1} = T_{N-1}$. Equation (1.21) would then be

$$(1 + \alpha c_N)T_N^{n+1} - \alpha c_N T_{N-1}^{n+1} = (1 - \alpha c_N)T_N^n + \alpha c_N T_{N-1}^n \quad (1.23)$$

However, c_N is ill-defined at $r_N = 0$. At the center, $T(r) = T(0) + \beta r^2/2$. Hence, $\partial T/\partial r = \beta r$ and $\partial^2 T/\partial r^2 = \beta$. The divergence of the temperature is

$$\nabla^2 T = \frac{1}{r^2} \frac{\partial}{\partial r} \left(r^2 \frac{\partial T}{\partial r} \right) = \frac{2}{r} \frac{\partial T}{\partial r} + \frac{\partial^2 T}{\partial r^2} = \frac{2}{r} \beta r + \beta = 3\beta = 3 \frac{\partial^2 T}{\partial r^2}$$

The divergence at the center can thus be evaluated as

$$(\nabla^2 T)_N = 3 \frac{T_{N+1} - 2T_N + T_{N-1}}{(\Delta r)^2} = 6 \frac{-T_N + T_{N-1}}{(\Delta r)^2}$$

and $(\text{rhs})_N$ is κ times this divergence. The lower boundary condition for the semi-implicit scheme becomes

$$(1 + 3\alpha)T_N^{n+1} - 3\alpha T_{N-1}^{n+1} = (1 - 3\alpha)T_N^n + 3\alpha T_{N-1}^n \quad (1.24)$$

In other words, $c_N = 3$, in equation (1.23). For comparison, $c_{N-1} = 5/4$.

Table 1.1: Current implementations of 1D heat equation solvers. `conductionT/Q` are provided in four languages: Fortran, C, Matlab, and Python.

Subroutine	Description
<code>conductionT.f90</code>	standard Crank-Nicolson solver
<code>conductionQ.f90</code>	Crank-Nicolson with σT^4 emission at upper boundary
<code>conductionT2.f90</code>	version of <code>conductionT</code> that precomputes coefficients
<code>conductionQ2.f90</code>	version of <code>conductionQ</code> that precomputes coefficients
<code>sphere1d_implicit.f90</code>	Crank-Nicolson solver for spherical geometry

Bibliography

- Handelsman, R. A. and Olmstead, W. E., 1972. Asymptotic solution to a class of nonlinear Volterra integral equations. *SIAM J. Appl. Math.* 22(3):373–384. doi: 10.1137/0122035.
- Kieffer, H. H., Martin, T. Z., Peterfreund, A. R., Jakosky, B. M., Miner, E. D., and Palluconi, F. D., 1977. Thermal and albedo mapping of Mars during the Viking primary mission. *J. Geophys. Res.* 82(28):4249–4291. doi: 10.1029/JS082i028p04249.
- Lide, D. R., editor, 2003. *CRC Handbook of Chemistry and Physics*. CRC Press, 84th edition.
- Schorghofer, N., 2008. Temperature response of Mars to Milankovitch cycles. *Geophys. Res. Lett.* 35:L18201. doi: 10.1029/2008GL034954.
- Schorghofer, N. and Aharonson, O., 2005. Stability and exchange of subsurface ice on Mars. *J. Geophys. Res.* 110(E5):E05003. doi: 10.1029/2004JE002350.

- Siegler, M., Aharonson, O., Carey, E., Choukroun, M., Hudson, T., Schorghofer, N., and Xu, S., 2012. Measurements of thermal properties of icy Mars regolith analogs. *J. Geophys. Res.* 117:E03001. doi: 10.1029/2011JE003938.
- Winter, D. F. and Saari, J. M., 1969. A particulate thermophysical model of the lunar soil. *Astrophys. J.* 156:1135–1151.

Part 2

Diffusion of Water Vapor with Phase Transitions

1-Dimensional Diffusion of Water Vapor in Porous Medium with Phase Transitions;
variable diffusivity; irregular grid

3 phases: vapor, free (macroscopic) H₂O ice, H₂O adsorbate
implemented in `vapordiffusioni.f`

History: developed 2003–2004

2.1 Governing Equations

indices: v ... gas (vapor), f ... free ice (solid), a ... adsorbed water
 $\bar{\rho}$... mass per total volume, \bar{J} ... vapor flux per total area

conservation of mass:

$$\frac{\partial}{\partial t}(\bar{\rho}_v + \bar{\rho}_f + \bar{\rho}_a) + \nabla \cdot \bar{J} = 0 \quad (2.1)$$

vapor transport: (Landau and Lifshitz, 1987, Vol. VI, §57, §58)

$$J = -D\rho_0\nabla c \quad (2.2)$$

c ... concentration $c = \rho_v/\rho_0$

ρ_{air} ... total density of air, including humidity

ρ_v ... density of vapor

$$p_v = nkT = \rho_v \frac{k}{m_v} T \quad (2.3)$$

m ... mass of molecule; k ... Boltzmann constant

adsorption: $\bar{\rho}_a = A(p, T)$

ϵ ... porosity (= void space / total volume)

$\epsilon(1 - \rho_f/\rho_{\text{ice}})$... fraction of space available to gas

$\bar{\rho}_v = \rho_v\epsilon(1 - \rho_f/\rho_{\text{ice}})$ ρ_v ... vapor density in void space

$\bar{\rho}_f = \rho_f\epsilon$ ρ_f ... ice density in volume not occupied by regolith

$\bar{J} = J\epsilon(1 - \rho_f/\rho_{\text{ice}})$ J ... vapor flux through void area
 $\rho_{\text{ice}} \approx 926 \text{ kg/m}^3$... density of ice when it's really cold

Conservation of mass becomes

$$\frac{\partial}{\partial t} \left(\rho_v \left(1 - \frac{\rho_f}{\rho_{\text{ice}}} \right) + \rho_f + \frac{1}{\epsilon} \bar{\rho}_a \right) + \partial_z \left(1 - \frac{\rho_f}{\rho_{\text{ice}}} \right) J = 0$$

$$\frac{\partial}{\partial t} \left[\rho_v \left(1 - \frac{\rho_f}{\rho_{\text{ice}}} \right) + \rho_f + \frac{1}{\epsilon} \bar{\rho}_a \right] = \partial_z \left[\left(1 - \frac{\rho_f}{\rho_{\text{ice}}} \right) D \partial_z \rho_v \right]$$

introduce $\varphi = 1 - \frac{\rho_f}{\rho_{\text{ice}}}$ and $\gamma = \frac{k}{m} \frac{1}{\epsilon}$

$$\partial_t \left(\frac{p}{T} \varphi + \frac{k}{m_v} \rho_f \right) + \gamma \left(\frac{\partial \bar{\rho}_a}{\partial p} \partial_t p + \frac{\partial \bar{\rho}_a}{\partial T} \partial_t T \right) = \partial_z \left[D \varphi \left(\partial_z \frac{p}{T} \right) \right] \quad (2.4)$$

This is an equation for p and ρ_f .

If there is no ice, then

$$\left(\frac{1}{T} + \gamma \frac{\partial \bar{\rho}_a}{\partial p} \right) \partial_t p + \left(-\frac{p}{T^2} + \gamma \frac{\partial \bar{\rho}_a}{\partial T} \right) \partial_t T = \partial_z \left(D \partial_z \frac{p}{T} \right)$$

2.2 Discretizations

2.2.1 Possible discretizations of spatial derivatives

Note: These spatial discretizations are not necessarily optimal in terms of discretization error.

$$\partial_z(a \partial_z b)|_j = \frac{1}{\Delta z^2} (a_{j+1/2}(b_{j+1} - b_j) - a_{j-1/2}(b_j - b_{j-1})) + O(\Delta z^2) \quad (2.5)$$

or

$$\partial_z(a \partial_z b)|_j = \frac{1}{2\Delta z^2} ((a_{j+1} + a_j)(b_{j+1} - b_j) - (a_j + a_{j-1})(b_j - b_{j-1})) + O(\Delta z^2) \quad (2.6)$$

or

$$\begin{aligned} \partial_z(a \partial_z b)|_j &= a \partial_{zz} b + (\partial_z a) \partial_z b \\ &= \frac{1}{\Delta z^2} \left[a_j(b_{j+1} - 2b_j + b_{j-1}) + \frac{1}{4}(a_{j+1} - a_{j-1})(b_{j+1} - b_{j-1}) \right] + O(\Delta z^2) \end{aligned} \quad (2.7)$$

The most general discretization which is accurate to $O(\Delta z^2)$, rather than just $O(\Delta z)$, is of the following form (mathematica notebook discretization2.nb)

$$\begin{aligned}\partial_z(a\partial_z b)|_j &= \frac{1}{\Delta z^2}(ca_j b_j + (-1 - \frac{c}{2})a_{j-1}b_j + (-1 - \frac{c}{2})a_{j+1}b_j \\ &\quad - \frac{c}{2}a_j b_{j-1} + \frac{3+c}{4}a_{j-1}b_{j-1} + \frac{1+c}{4}a_{j+1}b_{j-1} \\ &\quad - \frac{c}{2}a_j b_{j+1} + \frac{1+c}{4}a_{j-1}b_{j+1} + \frac{3+c}{4}a_{j+1}b_{j+1}) + O(\Delta z^2)\end{aligned}\quad (2.8)$$

Choices (2.6) and (2.7) above correspond to $c = -1$ and $c = -2$, respectively.

Another set of schemes does not involve the cross-terms $a_{j+1}b_{j-1}$ and $a_{j-1}b_{j+1}$. They are of the following form (mathematica notebook discretization3.nb)

$$\begin{aligned}\partial_z(a\partial_z b)|_j &= \frac{1}{\Delta z^2}(-a_j b_j - ca_{j-1}b_j + (-1+c)a_{j+1}b_j + \\ &\quad (1-c)a_j b_{j-1} + ca_{j-1}b_{j-1} + ca_j b_{j+1} + (1-c)a_{j+1}b_{j+1}) + \\ &\quad \left(c - \frac{1}{2}\right) O(\Delta z) + O(\Delta z^2) \\ &= \frac{1}{\Delta z^2}[(1-c)a_{j+1}(b_{j+1} - b_j) + ca_{j-1}(b_{j-1} - b_j) + \\ &\quad + a_j(cb_{j+1} - b_j + (1-c)b_{j-1})] + O(\Delta z)\end{aligned}\quad (2.9)$$

For $c = 1/2$ this reduces to scheme (2.6) above

If starting with complete pore filling, $c > 0$ is required for downward motion of ice table.

On irregular grid: General scheme without cross-terms (mathematica notebook discretization6.nb)

$$\begin{aligned}\partial_z(a\partial_z b)|_j &= -\frac{2c + (1-2c)h_+/h_-}{h_-h_+}a_j b_j + \frac{-1 + (1-2c)h_+/h_-}{h_-(h_- + h_+)}a_{j-1}b_j + \frac{2c-2}{h_+(h_- + h_+)}a_{j+1}b_j + \\ &\quad + \frac{1 + (1-2c)h_+/h_-}{h_-(h_- + h_+)}a_j b_{j-1} + \frac{1 + (2c-1)h_+/h_-}{h_-(h_- + h_+)}a_{j-1}b_{j-1} + \frac{2c}{h_+(h_- + h_+)}a_j b_{j+1} \\ &\quad + \frac{2-2c}{h_+(h_- + h_+)}a_{j+1}b_{j+1} + O(h_+ + h_-)\end{aligned}\quad (2.10)$$

where $h_+ = z_{j+1} - z_j$ and $h_- = z_j - z_{j-1}$. For $h_+ = h_- = h$ this reduces to (2.9)

2.2.2 Discretization of time derivative

use eq. (2.4), $A \equiv f$

$$\begin{aligned}\frac{p_j^{n+1}}{T_j^{n+1}}\varphi_j^{n+1} - \frac{p_j^n}{T_j^n}\varphi_j^n + \frac{k}{\mu}\left(\rho_{f_j}^{n+1} - \rho_{f_j}^n\right) + \gamma \left.\frac{\partial f}{\partial p}\right|_j^n (p_j^{n+1} - p_j^n) + \\ + \gamma \left.\frac{\partial f}{\partial T}\right|_j^n (T_j^{n+1} - T_j^n) = \Delta t \left(\partial_z D\varphi \partial_z \frac{p}{T}\right)_j^n\end{aligned}\quad (2.11)$$

derivatives of the isotherm are not expanded to keep it linear

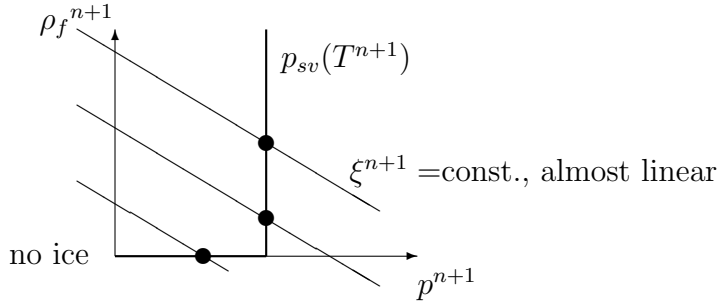
2.2.3 Complete scheme

using (2.11) and (2.10)

$$\begin{aligned}\xi_j^{n+1} = & \frac{p_j^n}{T_j^n} \varphi_j^n + \frac{k}{\mu} \rho_f^n + \gamma \left. \frac{\partial f}{\partial p} \right|_j^n p_j^n - \gamma \left. \frac{\partial f}{\partial T} \right|_j^n (T_j^{n+1} - T_j^n) + \\ & \frac{\Delta t}{\Delta z^2} \left[D_j \varphi_j^n \left(\frac{p_{j+1}^n}{T_{j+1}^n} - 2 \frac{p_j^n}{T_j^n} + \frac{p_{j-1}^n}{T_{j-1}^n} \right) + \frac{1}{4} (D_{j+1} \varphi_{j+1}^n - D_{j-1} \varphi_{j-1}^n) \left(\frac{p_{j+1}^n}{T_{j+1}^n} - \frac{p_{j-1}^n}{T_{j-1}^n} \right) \right]\end{aligned}$$

$$\text{where } \xi^{n+1} = \frac{p^{n+1}}{T^{n+1}} \left(1 - \frac{\rho_f^{n+1}}{\rho_{\text{ice}}} \right) + \frac{k}{\mu} \rho_f^{n+1} + \gamma \left. \frac{\partial f}{\partial p} \right|^n p^{n+1}$$

$$p \leq p_{sv}(T) \text{ and } 0 \leq \rho_f \leq \rho_{\text{ice}}$$



p_{sv} ... saturation vapor pressure

$$\text{Try } \rho_f^{n+1} = 0 \Rightarrow p^{n+1} = \frac{T^{n+1} \cdot \xi^{n+1}}{1 + T^{n+1} \gamma \left. \frac{\partial f}{\partial p} \right|^n} \text{ and } \rho_f^{n+1} = 0$$

$$\text{If } p^{n+1} > p_{sv}(T^{n+1}) \text{ then } p^{n+1} = p_{sv}(T^{n+1}) \text{ and}$$

$$\rho_f^{n+1} = \frac{\xi^{n+1} - \frac{p_{sv}(T^{n+1})}{T^{n+1}} - \gamma \left. \frac{\partial f}{\partial p} \right|^n p_{sv}(T^{n+1})}{\frac{k}{\mu} - \frac{p_{sv}(T^{n+1})}{T^{n+1} \rho_{\text{ice}}}}$$

$$\text{introduce } p_{\text{frost}}^{n+1} = p_{sv}(T^{n+1})$$

2.2.4 Upper boundary condition

- 1) $p(z=0, t) = p_{\text{atm.}}(t)$
- 2) $D(z=0) = D_0$
- 3) $\varphi_0 = 1$

$$\left. \partial_z \left(D \varphi \partial_z \frac{p}{T} \right) \right|_{j=0} = \frac{1}{\Delta z^2} \left[D_1 \varphi_1 \left(\frac{p_2}{T_2} - 2 \frac{p_1}{T_1} + \frac{p_{\text{atm}}}{T_{\text{surf}}} \right) + \frac{1}{4} (D_2 \varphi_2 - D_0 \varphi_0) \left(\frac{p_2}{T_2} - \frac{p_{\text{atm}}}{T_{\text{surf}}} \right) \right] \quad (2.12)$$

for half-shifted grid ($z_2 = 3z_1$):

$$a\partial_{zz}b + (\partial_z a)\partial_z b = \frac{1}{\Delta z^2} \left[a_1 \left(\frac{8}{3}b_s - 4b_1 + \frac{4}{3}b_2 \right) + \left(-\frac{4}{3}a_s + a_1 + \frac{1}{3}a_2 \right) \left(-\frac{4}{3}b_s + b_1 + \frac{1}{3}b_2 \right) \right] \quad (2.13)$$

2.2.5 Lower boundary condition

$$\text{no vapor flux (impermeable) } J = 0 \quad \Rightarrow \quad \partial_z \rho_v = 0 \quad \Rightarrow \quad \partial_z \frac{p}{T} = 0 \quad \Rightarrow \quad \frac{p_{N+1}}{T_{N+1}} = \frac{p_{N-1}}{T_{N-1}}$$

$$\partial_z \left(D\varphi \partial_z \frac{p}{T} \right) \Big|_{j=N} = \frac{1}{\Delta z^2} 2D_N \varphi_N \left(\frac{p_{N-1}}{T_{N-1}} - \frac{p_N}{T_N} \right) \quad (2.14)$$

2.3 Discussion

2.3.1 Numerical stability

von Neumann stability analysis has been carried out for various variants of the scheme; this is only relevant for discussion purposes. Typeset notes are available upon request.

2.3.2 Diffusion-advection

For 1D diffusion and advection with multiple gases, the governing equations are more complex, but the numerical implementation is not. For the governing equations in non-isothermal environments see works such as Cunningham and Williams (1980); Bouziani and Fanale (1998); Hudson et al. (2007).

Vapor diffusion calculations for Mars are carried out in Schorghofer and Aharonson (2005).

Bibliography

- Bouziani, N. and Fanale, F. P., 1998. Physical chemistry of a heterogeneous medium: Transport processes in comet nuclei. *Astrophys. J.* 499(1):463. doi: 10.1086/305599.
- Cunningham, R. and Williams, R., 1980. *Diffusion in Gases and Porous Media*. Plenum Press, New York.
- Hudson, T. L., Aharonson, O., Schorghofer, N., Farmer, C. B., Hecht, M. H., and Bridges, N. T., 2007. Water vapor diffusion in Mars subsurface environments. *J. Geophys. Res.* 112(E5):E05016. doi: 10.1029/2006JE002815.
- Landau, L. D. and Lifshitz, E. M., 1987. *Fluid Mechanics*. Pergamon Press, Oxford.
- Schorghofer, N. and Aharonson, O., 2005. Stability and exchange of subsurface ice on Mars. *J. Geophys. Res.* 110(E5):E05003. doi: 10.1029/2004JE002350.

Part 3

Long-Term Ice Evolution

Long-term evolution of sub-surface ice due to loss to space (for asteroids), vapor exchange with the atmosphere (for Mars), or exchange with adsorbed H_2O (on the Moon) using diurnally- and seasonally-resolved temperatures.

History:

2002–2004 equilibrium ice table on Mars

2006–2011 asynchronous model for ice on Mars (where re-charge can occur)

2013 lunar thermal ice pump

2013–2017 asynchronous model for asteroids (where impact-gardening occurs)

A computationally efficient treatment of the evolution of the ice volume near the surface of a planetary body is based on time-averaged equations for vapor transport.

3.1 Equilibrium Models of Near-Surface Ice on Mars

The equilibrium depth to the ice table is defined by a balance between the vapor pressure at the ice table and the atmosphere. It is the end result of atmosphere-subsurface vapor exchange after an asymptotically long time. If no equilibrium is possible, then subsurface ice is “unstable”. Using the thermal model described in Part 1, this model calculates the equilibrium depth based on matching the vapor density at the ice table with that in the atmosphere. The thermal model is run over a number of Mars years to equilibrate, and annual means are taken from the last orbit. The ice content of the subsurface changes the thermal properties, and the thermal model is repeatedly equilibrated. A root-finding procedure is deployed to find the equilibrium depth. In `mars_mapi.f` the root-finding procedure is a bisection method. The more recent but simpler program `mars_mapii.f` instead iteratively updates the instantaneous equilibrium depth to arrive at the unique final equilibrium depth. Then `mars_mapt.f` can be used to output additional variables for a given ice table depth.

The model is extensively used in Schorghofer and Aharonson (2005), where further description is available. With extensions described in section 5.2 for planar slopes, it also forms the core of the model used in Aharonson and Schorghofer (2006).

3.2 Asynchronous Model for Ice on Mars

Schorghofer (2010) provides a description of this rather complex model, which is not repeated here. In brief, the model couples a diurnally-resolved thermal model with a long-term ice evolution model. Ice (massive or interstitial) can be lost to the atmosphere and, vice-versa, pore spaces can be recharged with interstitial ice. Details of the long-term ice evolution model are also described in this paper, which involve a one-sided derivative at the moving ice table; otherwise a numerical instability occurs due to the strong contrast in thermal properties at the ice table. The model allows for up to three layers: ice-free, soil with interstitial ice (plus void spaces), and massive ice with dust. In the current implementation, one of the two interfaces is tracked explicitly. The model is extensively used in Schorghofer (2007) and Schorghofer and Forget (2012) for studies of the Martian Ice Age cycle.

3.3 Asynchronous Model for Temperature, Impact Mixing, and Ice Loss on Asteroids

Schorghofer (2016) describes this model and applies it to (1) Ceres and (7968) Elst-Pizarro. In brief, it combines diurnally-resolved temperatures, probabilistic impact stirring (only one-dimensional), and the long-term loss of near-surface ice to space. It was also used for the ice retreat calculations published in Prettyman et al. (2017). The solar constant gradually increases according to the standard solar evolution model (Gough, 1981). The main program is `asteroid_fast2`.

A significant complexity in this model arises from partially ice-filled pore spaces (necessary to incorporate the consequences of impact stirring), because the re-distribution of ice within the pores due to vapor diffusion and deposition adds another governing equation. This redistribution turned out to be negligible in all cases it was considered. A simpler two-layer version, where pore spaces are either empty or full, is implemented in `asteroid_fast1`, which is very similar to the model described in the supporting information of Sizemore et al. (2017).

Another application of asynchronous coupling is ice loss calculations for asteroids on dynamical orbits, that is, the orbital elements change over time (and continuous-time integration would be too slow). In Schorghofer et al. (2020) this computational method was applied to (potentially ice-rich) asteroids that originate in the Outer Main Belt.

3.4 Lunar Thermal Ice Pump

The concept of downward “pumping” of vapor by periodic temperature cycles, originally developed for Mars, can also be applied to the Moon, as described in Schorghofer and Taylor (2007); Schorghofer and Aharonson (2014). The governing equations are cast in the form of a boundary value problem, that is, by calculating the mobility of H_2O molecules on the surface and at one specific depth. One component of these calculations is a model for the surface population of adsorbed water molecules. It involves a stiff differential equation that is solved with a simple implicit method (a backward Euler step). The “bottom point” is the ice table,

Table 3.1: Overview of current implementations of asynchronous models

Main program	Task
<code>mars_mapi</code>	finds equilibrium ice table with bisection method
<code>mars_mapii</code>	finds equilibrium ice table with iteration method
<code>mars_mapt</code>	temperatures for prescribed ice table depth
<code>mars_mapi2p</code>	finds equilibrium ice table for planar slopes with bisection method
<code>mars_fast</code>	ice evolution on Mars (massive and interstitial ice)
<code>exper_fast</code>	ice evolution in lab experiment
<code>stabgrow_fast</code>	pore ice evolution in simple environment
<code>asteroid_fast1</code>	temperature, ice loss, collapsed sublimation lag
<code>asteroid_fast2</code>	temperature, ice loss, impact mixing

or, for the purpose of determining whether or not pumping occurs, the depth of minimum sublimation rate, which is estimated by the sublimation rate at time-averaged temperature. Program `oscidea1.f90` is a simple driver program for the ice pump calculations. This model was also used in Schorghofer and Williams (2020).

For the “adsorbate pump”, the pumping is too weak for ice sequestration, but the pumping nevertheless causes an increase of adsorbate concentration with depth. Subsurface residence times depend not only on temperature but also on adsorbate density, which requires nonlinear root-finding, in addition to the surface population model.

Bibliography

- Aharonson, O. and Schorghofer, N., 2006. Subsurface ice on Mars with rough topography. *J. Geophys. Res.* 111(E11):E11007. doi: 10.1029/2005JE002636.
- Gough, D. O., 1981. Solar interior structure and luminosity variations. *Solar Physics* 74: 21–34. doi: 10.1007/978-94-010-9633-1_4.
- Prettyman, T. H. et al., 2017. Extensive water ice within Ceres’ aqueously altered regolith: Evidence from nuclear spectroscopy. *Science* 355:55–59. doi: 10.1126/science.aah6765.
- Schorghofer, N., 2007. Dynamics of ice ages on Mars. *Nature* 449(7159):192–194. doi: 10.1038/nature06082.
- Schorghofer, N., 2010. Fast numerical method for growth and retreat of subsurface ice on Mars. *Icarus* 208(2):598–607. doi: 10.1016/j.icarus.2010.03.022.
- Schorghofer, N., 2016. Predictions of depth-to-ice on asteroids based on an asynchronous model of temperature, impact stirring, and ice loss. *Icarus* 276:88–95. doi: 10.1016/j.icarus.2016.04.037.
- Schorghofer, N. and Aharonson, O., 2005. Stability and exchange of subsurface ice on Mars. *J. Geophys. Res.* 110(E5):E05003. doi: 10.1029/2004JE002350.
- Schorghofer, N. and Aharonson, O., 2014. The lunar thermal ice pump. *Astrophys. J.* 788: 169. doi: 10.1088/0004-637X/788/2/169.

- Schorghofer, N. and Forget, F., 2012. History and anatomy of subsurface ice on Mars. *Icarus* 220(2):1112–1120. doi: 10.1016/j.icarus.2012.07.003.
- Schorghofer, N. and Taylor, G. J., 2007. Subsurface migration of H₂O at lunar cold traps. *J. Geophys. Res.* 112(E2):E02010. doi: 10.1029/2006JE002779.
- Schorghofer, N. and Williams, J.-P., 2020. Mapping of ice storage processes on the Moon with time-dependent temperatures. *Planet. Sci. J.* 1:54. doi: 10.3847/PSJ/abb6ff.
- Schorghofer, N., Hsieh, H. H., Novakovic, B., and Walsh, K. J., 2020. Preservation of ice at the polar regions of near-earth asteroids originating in the outer main asteroid belt: A model study with dynamical trajectories. *Icarus* 348:113865. doi: 10.1016/j.icarus.2020.113865.
- Sizemore, H. G. et al., 2017. Pitted terrain on dwarf planet Ceres and implications for volatiles. *Geophys. Res. Lett.* 44(13):6570–6578. doi: 10.1002/2017GL073970.

Part 4

Terrestrial Analogs

0-Dimensional Terrestrial Atmosphere, 3-Dimensional Insolation, 1-Dimensional Thermal Model

History:

2013–2016 Mauna Kea, Hawaii (sec. 4.1 and 5)

2004–2005 Beacon Valley, Antarctica (sec. 4.2)

Sun position as a function of date is based on Blanco-Muriel et al. (2001), translated into Fortran. It provides the zenith angle and azimuth of the sun, and the Earth-sun distance. Implemented in `sunpos.f90`

4.1 Mauna Kea atmosphere

clear-sky direct and indirect short-wave irradiance (W/m^2) on Mauna Kea

Parametrizations in the atmospheric model are mostly based on Nunez (1980), corrected for typos. Implemented in `mk_atmosphere.f90`

Z ... solar zenith angle (radians)

I_0 ... clear-sky direct irradiance; D_0 ... clear-sky diffuse irradiance

R ... Earth-sun distance in AU

m, m' ... optical air mass (unitless)

p_0 ... total pressure (Pa)

w ... precipitable water vapor (cm)

Transmission coefficients:

ψ_{wa} ... water vapor absorption; ψ_{ws} ... water vapor scattering

ψ_{rs} ... Rayleigh scattering

ψ_{da} ... dust absorption; ψ_{ds} ... dust scattering

Relative air mass:

simplest approximation: $m = 1/\cos Z$

better approximation (Kasten, 1966):

$$m = \frac{1}{\cos Z + 0.15 \times (93.885 - Z)^{-1.253}} \quad (4.1)$$

if ($m < 0$), then $m = \infty$
 $p_0 = 610$ on Mauna Kea summit
 $m' = m \times p_0/1013$

Water vapor:

$w = 0.16$ cm for Mauna Kea, according to www.gemini.edu/sciops/telescopes-and-sites/observing-condition-constraints/mk-water-vapour-statistics

$$\psi_{wa} = 1 - 0.077(wm)^{0.30} \quad \text{McDonald (1960)} \quad (4.2)$$

$$\psi_{ws} = 1 - 0.025wm \quad (4.3)$$

Rayleigh scattering: 8% at sea level according to Fig 3-3 in Bird and Hulstrom (1981)

$$\psi_{rs} = \exp(-0.08m') \quad (4.4)$$

Aerosols: aerosol optical depth on Mauna Kea = $0.0084 \times (\lambda/1\mu\text{m})^{-1.26}$ (Buton et al., 2013)

$$\psi_{ds} = \exp(-m \times 0.0084 \times 0.5^{-1.26}) \quad (4.5)$$

$$\psi_{da} = \psi_{ds} \quad \text{assumes single scattering albedo of 0.5} \quad (4.6)$$

Direct sunlight:

$$I_0 = \psi_{wa}\psi_{da}\psi_{ws}\psi_{rs}\psi_{ds} \times (\text{solar constant})/R^2 \quad (4.7)$$

(without the last factor, this is the transmittance)

Diffuse sunlight:

$$D_0 = I_0 \cos(Z) \psi_{wa} \psi_{da} \frac{1 - \psi_{ws} \psi_{rs} \psi_{ds}}{2} \quad (4.8)$$

Roundoff issue: if ($D_0 \leq 0$), then $D_0 = 0$ because of -0 .

Total short-wavelength flux:

$$F = I_0 \cos Z + D_0 \quad (4.9)$$

Roundoff issue: if ($F \leq 0$), then $F = 0$ because of -0 .

Not included are the sensible heat flux and long-wave downward radiation.

Atmospheric contribution with terrain shadowing: see section 5.6 and references therein.

used in Schorghofer et al. (2017) and Schorghofer (2018)

4.2 Dry Valleys of Antarctica

This model calculates the loss of buried ice to the atmosphere, and involves molecular diffusion in an air-H₂O mixture, including the advective contribution. The equations underlying this model are described in Schorghofer (2005). The source code has not been readied for distribution and no further documentation was written. By now this model has been superseded by more capable implementations from other research groups.

Bibliography

- Bird, R. E. and Hulstrom, R. L., 1981. A simplified clear sky model for direct and diffuse insolation on horizontal surfaces. Technical report, Golden, Colorado. Report No. SERI/TR-642-761.
- Blanco-Muriel, M., Alarcón-Padilla, D. C., López-Moratalla, T., and Lara-Coira, M., 2001. Computing the solar vector. *Solar Energy* 70:431–441. doi: 10.1016/S0038-092X(00)00156-0.
- Buton, C. et al., 2013. Atmospheric extinction properties above Mauna Kea from the Nearby SuperNova Factory spectro-photometric data set. *Astron. Astrophys.* 549:A8. doi: 10.1051/0004-6361/201219834.
- Kasten, F., 1966. Albedo and sky radiance measurements in Greenland. *Arch. Meteor. Geophys. Bioklimatol.* B14:206–223. <http://hdl.handle.net/11681/5813>.
- McDonald, J. E., 1960. Direct absorption of solar radiation by atmospheric water vapor. *Journal of Meteorology* 17:319–328. doi: 10.1175/1520-0469(1960)017%3C0319:DAOSRB%3E2.0.CO;2.
- Nunez, M., 1980. The calculation of solar and net radiation in mountainous terrain. *Journal of Biogeography* 7:173–186. doi: 10.2307/2844709.
- Schorghofer, N., 2005. A physical mechanism for long-term survival of ground ice in Beacon Valley, Antarctica. *Geophys. Res. Lett.* 32:L19503. doi: 10.1029/2005GL023881.
- Schorghofer, N., 2018. Permafrost survey on the Maunakea summit plateau: Final report. Technical report, University of Hawaii. 28pp.
- Schorghofer, N., Leopold, M., and Yoshikawa, K., 2017. State of high-altitude permafrost on tropical Maunakea volcano, Hawaii. *Permafrost and Periglacial Processes* 28:685–697. doi: 10.1002/ppp.1954.

Part 5

3D Surface Energy Balance

Energy Balance with Terrain Shadowing, Terrain Irradiance, and Sky Irradiance

History:

2002–2005 Planar slopes (sec. 5.1 & 5.2)

2010–2019 3D topography (sec. 5.3–5.7)

With 3-dimensional topography the surface energy balance is modified, compared to a horizontal unobstructed planar surface, for the following reasons:

DIRECT IRRADIANCE:

- 1) changed incidence angle
- 2) elevated horizons (terrain shadowing)

TERRAIN IRRADIANCE:

- 3) reflected sunlight from visible land surfaces
- 4) infrared emissions from visible land surfaces (“self-heating”)

SKY IRRADIANCE (for bodies with atmospheres):

- 5) restricted diffuse sky irradiance (short-wavelength and long-wavelength)

The incidence angle on a sloped surface is easily calculated. The elevated horizons change the time of sunset and sunrise, and also reduce the irradiance received from the atmosphere. Horizon determinations require that all other pixels in the domain are considered, so this is a non-local computational problem. Diffusively reflected sunlight and infrared emissions are also known as “terrain irradiance” and require the evaluation of “view factors”. Calculating the terrain irradiance is computationally even more demanding than the horizons calculations.

5.1 Incidence Angle on Slope

The elevation β of the sun above a horizontal horizon is given in terms of geographic latitude λ , declination δ of the sun, and the hour angle h by

$$\sin \beta = \cos \lambda \cos \delta \cos h + \sin \lambda \sin \delta. \quad (5.1)$$

The angle θ of the sun above a sloped surface is

$$\sin \theta = \cos \alpha \sin \beta - \sin \alpha \cos \beta \cos(\Delta a), \quad (5.2)$$

where α is the slope angle and Δa is the difference between the azimuth of the sun and the azimuth of the topographic gradient. The sun is assumed to be below the horizon if either $\sin \beta < 0$ (horizontal horizon at infinity) or $\sin \theta < 0$ (self shadowing of slope). For 3D topography, a distant horizon, higher than the self shadowing slope, introduces an additional cutoff e_{\max} (horizon elevation).

On an airless body the direct insolation is

$$Q_{\text{solar}} = \frac{S_0}{R^2} (1 - A) \sin \theta. \quad (5.3)$$

where S_0 is the solar constant, R the distance from the sun in AU, and A the albedo.

5.2 Thermal Model for Tilted Planar Slope

Planar slopes are much simpler than the general 3D problem. This section describes a model for the thermal balance on a tilted plane, in the form of two coupled 1D thermal models, plus a 0D atmosphere. The model is for Mars, but easily simplified to airless bodies. It was used in Aharonson and Schorghofer (2006) and Schorghofer and Edgett (2006).

Let α denote the slope angle. The heat balance on the surface is

$$Q(\alpha) + k \left. \frac{\partial T}{\partial z} \right|_{z=0} = \epsilon \sigma T^4 + (\text{latent heat of CO}_2 \text{ frost}) \quad (5.4)$$

with

$$Q = Q_{\text{solar}}(\alpha) + Q_{\text{a,IR}}(\alpha) + Q_{\text{a,scat}}(\alpha) + Q_{\text{land}}(\alpha). \quad (5.5)$$

Q is the incoming radiation from the sun, atmosphere, and surfaces within field of view, T temperature, z the vertical coordinate, k the thermal conductivity, ϵ emissivity, and σ the Stefan-Boltzmann constant. The subscript a denotes contributions from the atmosphere. Figure 5.1 illustrates the contributions.

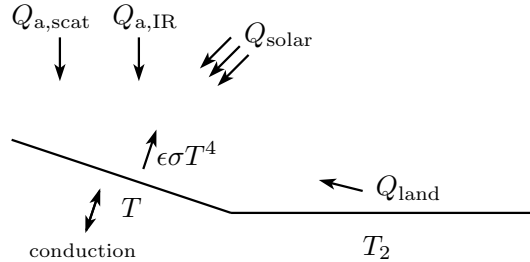


Figure 5.1: Contributions to the heat balance on a slope with surface temperature T .

For Mars, the direct solar insolation is

$$Q_{\text{solar}} = \frac{S_0}{R^2} (1 - A) (1 - f)^{1/\max(\sin \beta, 0.04)} \sin \theta, \quad (5.6)$$

where f due to the extinction in the atmosphere. This is a generalization of (1.11). The length of the path through the atmosphere is proportional to $1/\sin\beta$. The maximum atmospheric path length is limited due to the curvature of the planet, which motivates the threshold of 0.04, as described in subsection 1.2.3.

The calculation of the atmospheric absorption and scattering is modified from subsection 1.2.3 to involve a prefactor of $\cos^2(\alpha/2)$. This slope factor for the IR emission takes into account the restricted size of the visible sky. Equations (1.12) and (1.13) become:

$$Q_{a,IR} = f_{IR} \frac{S_0}{R^2} \cos^2\left(\frac{\alpha}{2}\right) \sin\beta_{\text{noon}} \quad (\text{all day}) \quad (5.7)$$

$$Q_{a,scat} = \frac{1}{2} f_{scat} \frac{S_0}{R^2} \cos^2\left(\frac{\alpha}{2}\right) \quad \text{when } \sin\beta > 0 \quad (5.8)$$

See section 5.6 and Flo Heggem et al. (2001) for other types of parametrizations. Spiga and Forget (2008) have derived a more detailed parameterization for $Q_{a,scat}$ on a planar slope.

The surface reemits radiation in all directions, but receives additional energy from surfaces in its field of view (terrain irradiance). This emission is weighted according to the incidence angle ι (Greek letter iota) and integrated over the spherical angle Ω subtended by the visible land surfaces. If we consider a horizontal surface at uniform temperature T_2 (Kreslavsky and Head, 2005):

$$Q_{\text{land}} = \epsilon_2 \sigma T_2^4 \int \cos\iota d\Omega = \sin^2\left(\frac{\alpha}{2}\right) \epsilon_2 \sigma T_2^4. \quad (5.9)$$

If one assumes $T_2 = T$ and $\epsilon_2 = \epsilon$, then this term can be brought to the right-hand side of eq. (5.4), leading to an effective emissivity of $\epsilon \cos^2(\alpha/2)$. However, this is often not a good approximation, as demonstrated in Aharonson and Schorghofer (2006), Fig. 2b. It is more accurate to base T_2 on a separate 1D model for a flat surface.

5.3 Horizons and Multigrids (Terrain Shadowing)

Shadowing by nearby topography (terrain shadowing) defines local horizons and is important for the energy balance. Horizons for each pixel are determined with azimuth rays, typically every 2° in azimuth, and the highest horizon in each direction is stored. For the purpose of horizon determination, the topography is represented by triangular facets. The horizon-finding calculation is implemented in `shadows.f90` and `shadow_subs.f90`.

The topography is defined on a rectangular coordinate grid with spatial resolution Δx in the longitude direction and Δy in the latitude direction. Curvature effects are not incorporated, i.e., the domain needs to be small compared to the radius of the body. Nor can the domain include the rotational pole. Surface normals are calculated using center-differences in x - and y -direction, and one-sided differences at the domain boundaries.

Multigrid Acceleration for Horizons Calculations: Use of spatial grids with various resolutions (multigrid method) dramatically accelerates the horizons calculation, because cells that are far from the point of interest are larger and fewer (Figure 5.2). For a domain with $N \times N$ pixels, the computational cost without multigrid method is $O(N^4)$. With multigrid, it is $O(N^2 \log N)$. In the current implementation of the multigrid method, up to ten grids

can be used; the difference in resolution between the coarsest and finest grids is a factor of 2^{10-1} . If the multigrid method is not used, an optional cut-off radius **RMAX** can be introduced, so spatial distances larger than **RMAX** are ignored.

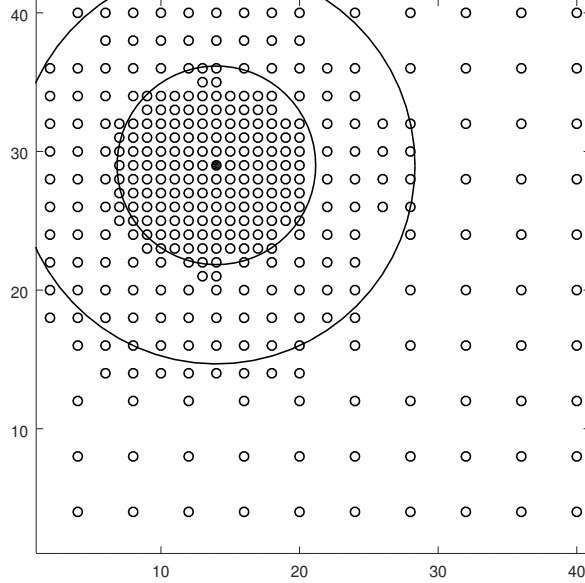


Figure 5.2: Example of multigrid (empty dots) used to determine horizons for one point of interest (solid dot). A progressively downsampled topography is used as the distance from the point of interest increases. This example uses three levels of grids.

First, grids of various resolutions are created, until the coarsest grid consists of only a few pixels along the narrower side of the rectangular domain. Grid coordinates of the coarse cells are also grid coordinates on the finest grid. Progressive downsampling by factors of two involves weighted averaging among the 8 nearest neighbors and the center point itself, such that $\iint h(x,y)dx dy$ is conserved (other than at the edges of the domain).

The determination of the grid points to be used for each point of interest begins by looping through the coarsest grids. If the distance of the center point to the point of interest is too small, the algorithm proceeds by looping through the four finer cells that make up the coarse cell. This is done recursively, until the resolution is appropriate for the distance or the finest grid is reached. This results in multigrids as in Figure 5.2.

5.4 Governing Equations with Terrain Irradiance

The equation governing the energy balance on the surface on an airless body is

$$(1 - A)(Q_{\text{direct}} + Q_{\text{refl}}) + k \frac{\partial T}{\partial z} + \epsilon Q_{\text{IR}} = \epsilon \sigma T^4 \quad (5.10)$$

where A is albedo, Q_{direct} incoming solar radiation (insolation), k thermal conductivity, T temperature, z depth below surface, ϵ emissivity, and σ the Stefan-Boltzmann constant. The flux Q_{direct} is determined from the declination of the Sun, latitude, and hour angle, eqs. (5.1,

5.2). Due to topography, reflected sunlight (Q_{refl}) and thermal emission (Q_{IR}) from other surfaces need to be added.

The diffuse terrain irradiance depends on the spherical angle $d\Omega$ subtended by the facet, and similarly for infrared emission:

$$Q_{\text{refl}}(x, y) = \frac{1}{\pi} \iint A' [Q'_{\text{direct}} + Q'_{\text{refl}}] \cos \iota d\Omega(x, y, x', y') \quad (5.11)$$

$$Q_{\text{IR}}(x, y) = \frac{1}{\pi} \iint [\epsilon \sigma T'^4 + (1 - \epsilon) Q'_{\text{IR}}] \cos \iota d\Omega(x, y, x', y') \quad (5.12)$$

where primed variables are evaluated at (x', y') and unprimed variables at (x, y) . The integrals are over all facets within the field of view, and ι is the angle between the surface normal and the line of sight that connects the two facets. The term with the factor $(1 - \epsilon)$ is reflected infrared.

In the literature these equations are often written in terms of a “view factor”

$$V_{ij} = \frac{\cos \iota_i \cos \iota_j}{\pi r_{ij}^2} d\mathcal{A}_j \quad (5.13)$$

where r_{ij} is the distance between the two facets, $\iota_i = \iota(x, y)$, $\iota_j = \iota(x', y')$, and $d\mathcal{A}$ the differential surface area. Since

$$d\Omega = \frac{\cos \iota_j}{r_{ij}^2} d\mathcal{A}_j$$

this is equivalent. The discretized equations then take the form

$$Q_{\text{refl } i} = \sum_{j'} A_{j'} [Q_{\text{direct } j'} + Q_{\text{refl } j'}] V_{i, j'} \quad (5.14)$$

$$Q_{\text{IR } i} = \sum_{j'} [\epsilon \sigma T_{j'}^4 + (1 - \epsilon) Q_{\text{IR}, j'}] V_{i, j'} \quad (5.15)$$

Equations (5.11) and (5.12) are linear equations for Q_{refl} and Q_{IR} , widely known as radiosity equations. However, for a time-dependent problem with subsurface heat conduction, it is not necessary to solve the radiosity equations. Instead, these equations can be used as explicit time-stepping procedure with Q_{refl} , T , and Q_{IR} on the right hand side evaluated at the previous time step n , whereas Q_{direct} and A can be evaluated at time step $n + 1$.

5.5 View Factors

Mutual visibility is determined by calculating the slope of the line that connects the two surface facets and comparing it to the maximum topographic slope along a ray in the same direction, tracing outward. (Hence there is a sort involved that is not necessary if only horizons are needed.)

Ultimately, the view factor of all mutually visible facets is calculated and stored. For the purpose of view factors, the topography is represented by rectangles. The visibility and view factor calculations are implemented in `fieldofviews.f90` and `fieldofview_subs.f90`.

View factor values can be validated for a bowl-shaped crater (a spherical cap). Inside a sphere of radius R

$$\frac{\cos \iota_i \cos \iota_j}{r_{ij}^2} = \frac{\cos^2 \iota}{(2R \cos \iota)^2} = \frac{1}{4R^2} \quad (5.16)$$

for any pair of facets i, j . The viewfactor (5.13) is therefore $V_{ij} = d\mathcal{A}_j/(4\pi R^2)$.

The differential solid angle can be written as

$$d\Omega = \cos e \, de \, d\varphi \quad (5.17)$$

where φ is azimuth and e the elevation (an angle) above the horizon. The solid angle of the entire landscape within field of view is

$$\Omega_{\text{land}} = \iint d\Omega = \int_0^{2\pi} \int_0^{e(\varphi)} de \, d\varphi \cos e = \int_0^{2\pi} d\varphi \sin(e(\varphi)) \quad (5.18)$$

The spherical angle of the visible sky is $\Omega_{\text{sky}} = 2\pi - \Omega_{\text{land}}$. It is also helpful to introduce the abbreviation

$$G = \frac{1}{\pi} \iint \cos \iota \, d\Omega \quad (5.19)$$

For a half-sphere $G = 1$.

Next several special cases, with increasing complexity, are considered:

- a) In the special case of a surface covered by a dome at uniform temperature,

$$\iint \cos \iota \, d\Omega = \int_0^{2\pi} d\varphi \int_0^{\pi/2} de \sin e \cos e = 2\pi \int_0^{\pi/2} de \sin e \cos e = 2\pi \frac{1}{2} \sin^2(\pi/2) = \pi$$

Hence $G = 1$ and (5.12) becomes $Q_{\text{IR}} = \epsilon \sigma T'^4$ (plus the reflected infrared, but the emissivity of the sky is different from the emissivity of the surface).

- b) Planar slope with a single temperature combined with a horizontal surface with another temperature, as in Figure 5.1. In this case, $\Omega = 2\alpha$, so that at $\alpha = \pi/2$ a quarter of the sphere remains. For the slope, the horizon height $e(\varphi)$ along direction φ is related by $\tan \alpha \cos \varphi = \tan e$.

For integration practice,

$$\begin{aligned} \iint d\Omega &= \int_{-\pi/2}^{\pi/2} d\varphi \int_0^{e(\varphi)} de \cos e = \int_{-\pi/2}^{\pi/2} d\varphi \sin(e(\varphi)) \\ &= \int_{-\pi/2}^{\pi/2} d\varphi \frac{\tan \alpha \cos \varphi}{\sqrt{1 + \tan^2 \alpha \cos^2 \varphi}} = 2\alpha \end{aligned}$$

where $\sin e = \tan e / \sqrt{1 + \tan^2 e}$ was used. The integral of interest

$$\begin{aligned} \iint \cos \iota \, d\Omega &= \int_{-\pi/2}^{\pi/2} d\varphi \int_0^{e(\varphi)} de \sin e \cos e \\ &= \int_{-\pi/2}^{\pi/2} d\varphi \frac{1}{2} \sin^2(e(\varphi)) = \frac{1}{2} \int_{-\pi/2}^{\pi/2} d\varphi \frac{\tan^2 \alpha \cos^2 \varphi}{1 + \tan^2 \alpha \cos^2 \varphi} \\ &= \frac{\pi}{2} (1 - \cos \alpha) = \pi \sin^2 \left(\frac{\alpha}{2} \right) \end{aligned}$$

In this case, $G = \sin^2(\alpha/2)$ and (5.12) becomes

$$Q_{\text{IR}} = \epsilon \sigma T'^4 \sin^2\left(\frac{\alpha}{2}\right) \quad (5.20)$$

plus the reflected infrared, which reproduces (5.9).

c) Uniform temperature, locally flat:

$$\iint \cos \iota \, d\Omega = \int_0^{2\pi} \int_0^{e(\varphi)} de \, d\varphi \cos e \sin e = \frac{1}{2} \int_0^{2\pi} d\varphi \sin^2(e(\varphi))$$

G equals $\sin^2 e(\varphi)$ averaged over azimuths. For small e , $G \ll \Omega_{\text{land}}/(2\pi)$.

d) Uniform temperature, not locally flat:

$$\sin \theta = \cos \iota = \cos \alpha \sin \beta + \sin \alpha \cos \beta \cos(\Delta a)$$

where α is the local slope angle. There is now also a lower limit on the elevation angle, $e_{\min}(\varphi)$, from the self-shadowing of the slope, so $\sin \theta$ will never become negative, and therefore

$$\tan e_{\min} = -\tan \alpha \cos(\Delta a)$$

which can be positive or negative.

The integral of interest is

$$\iint \cos \iota \, d\Omega = \int_0^{2\pi} \int_{e_{\min}(\varphi)}^{e(\varphi)} de \, d\varphi \cos e [\cos \alpha \sin e + \sin \alpha \cos e \cos(\Delta a)] \quad (5.21)$$

and the integrals over e can be computed as

$$\begin{aligned} \frac{1}{\pi} \int de \cos e \sin e &= \frac{1}{2\pi} \sin^2 e \\ \frac{1}{\pi} \int de \cos^2 e &= \frac{1}{2\pi} (e + \sin e \cos e) \end{aligned}$$

G can be pre-computed from static geometric information:

$$\begin{aligned} G &= \frac{\cos \alpha}{2\pi} \int_0^{2\pi} d\varphi (\sin^2 e - \sin^2 e_{\min}) + \\ &\quad + \frac{\sin \alpha}{2\pi} \int_0^{2\pi} d\varphi \cos(\Delta a) (e + \sin e \cos e - e_{\min} - \sin e_{\min} \cos e_{\min}) \end{aligned} \quad (5.22)$$

An approximation for small e is

$$G \approx \frac{\sin \alpha}{\pi} \int_0^{2\pi} d\varphi \cos(\Delta a) (\sin e - \sin e_{\min})$$

For comparison, the surface area (in steradian) visible from an inclined surface is

$$\Omega_{\text{land}} = \iint d\Omega = \int_0^{2\pi} \int_{e_{\min}(\varphi)}^{e(\varphi)} de \, d\varphi \cos e = \int_0^{2\pi} d\varphi (\sin e - \sin e_{\min}) \quad (5.23)$$

Equations (5.12) and (5.22) invite a particularly useful approximation for the terrain irradiance. Assuming all land within field of view has the same surface temperature, Q_{IR} can be calculated from G and view factors for individual facets are not required. One choice for the uniform temperature is the (time-dependent) surface temperature of a horizontal and unobstructed surface. Similarly, Q_{refl} can be calculated the same way when assuming AQ_{direct} is uniform on land within the field of view. After horizons and G have been calculated, the surface energy balance calculations for each pixel are independent of one another, and the entire model implementation can be easily parallelized.

5.6 Diffuse Sky Irradiance in the Presence of Horizons

For bodies with atmosphere, the diffuse irradiance from the sky is assumed to be isotropic (Lambertian), both for short-wave and long-wavelength radiation. In the literature more than one definition of (sky) view factor and various approximations for the sky irradiance are in use; see Flo Heggem et al. (2001) and Rakovec and Zakšek (2012).

The sky view factor F_{sky} is the spherical angle of the visible sky divided by 2π . The size of the sky (between 0 and 2π steradian) can be calculated from either the horizon heights or the view factors of the landscape segments.

For Mars, in the spirit of the Kieffer approximation (subsection 1.2.3),

$$Q_{\text{a,IR}} = Q_0 F_{\text{sky}} f_{\text{IR}} \sin \beta_{\text{noon}} \quad (\text{all day}) \quad (5.24)$$

and if the sun is up, then

$$Q_{\text{a,scat}} = \frac{1}{2} Q_0 (1 - A) F_{\text{sky}} f_{\text{scat}} \quad \text{when } \sin \beta > 0 \quad (5.25)$$

otherwise $Q_{\text{a,scat}} = 0$.

The alternative is to weigh the diffuse irradiance from the atmosphere with the cosine of the incidence angle. This is the view factor V as defined above for land segments. The factor F_{sky} is to be replaced with G_{sky} in (5.24) and (5.25). For computing the sky view factor, eq. (5.22) can be used with e_{min} replaced by e , and e replaced by $\pi/2$:

$$G_{\text{sky}} = \frac{\cos \alpha}{2\pi} \int_0^{2\pi} d\varphi (1 - \sin^2 e) + \frac{\sin \alpha}{2\pi} \int_0^{2\pi} d\varphi \cos(\Delta a) \left(\frac{\pi}{2} - e - \sin e \cos e \right) \quad (5.26)$$

$$= \frac{\cos \alpha}{2\pi} \int_0^{2\pi} d\varphi \cos^2 e - \frac{\sin \alpha}{2\pi} \int_0^{2\pi} d\varphi \cos(\Delta a) (e + \sin e \cos e) \quad (5.27)$$

This equation can be found in Dozier and Frew (1990).

For a planar slope $F_{\text{sky}} = 1 - \alpha/2\pi$ and $G_{\text{sky}} = \cos^2(\alpha/2)$. The latter matches the approximation chosen in section 5.2.

For (high-elevation) regions on Earth (such as Mauna Kea), short-wavelength irradiance scattered or absorbed by the atmosphere is considered, as described in section 4.1.

5.7 Outline of Implementation

The calculations are separated into two parts.

The first, described in section 5.3, determines the horizons for all pixels and (optionally) view factors of all facets with all other facets. This information is written to files `horizons.dat` and `viewfactors.dat`, respectively. This part is easily parallelized, as calculations for each pixel are independent of one another although the entire topography has to be loaded into memory at once. For parallelization, one slice of the spatial domain is run on each CPU thread. It can be submitted to a computer cluster as an array job.

In the `horizons` file, each line is preceded by the integer pixel coordinates. The file is rectangular, and the number of entries is (number of azimuth rays + 2) × (number of topographic pixels). The `viewfactors` file is giant and it is not rectangular. Each line in the output file corresponds to a topographic pixel and at the beginning specifies the number of pixels within field of view. Each visible pixel has then three numbers stored with it: The two integer pixel coordinates and the view factor, V_{ij} , for this pixel. Non-visible pixels are not stored.

Horizons calculations are implemented in `shadows.f90` and its subroutines. If the view factors are desired, use `fieldofviews.f90`. Horizon heights are also calculated within `fieldofviews.f90`, but with a slightly different algorithm than in `shadows.f90`.

The second part simulates the time evolution of illumination and surface temperature as the sun moves through the sky, using the horizons and (optionally) the field of view as input. The horizons are read in a module called `newhorizons`, which also interpolates horizon elevations for any desired azimuth. The field of view information is read with a separate subroutine. To save memory, the pixel coordinates are stored as 2-byte integers and the view factors as 4-byte floating point numbers, respectively, half of the common byte lengths.

The surface energy balance is integrated over time at steps of a fraction (e.g., 1/50th) of a solar day. Surface temperature and illumination are updated at every time step. The names of the main programs start with `cratersQ_*` (Table 5.1).

Table 5.1: Overview of current implementations

Main program	Task	Reflections	Parallel
<code>shadows</code>	pre-calculate horizons, optional multigrid	N/A	yes
<code>fieldofviews</code>	pre-calculate view factors, no multigrid	N/A	yes
<code>insol3d_earth</code>	direct insolation only, Mauna Kea atm.	no	no
<code>insol3d_mars</code>	direct insolation only, no atmosphere	no	no
<code>cratersQ_equilbr</code>	equilibrium solution for airless body	yes	no
<code>cratersQ_moon</code>	airless body	yes	no
<code>cratersQ_mars</code>	Mars orbit and atmosphere	G-approx.	no
<code>cratersQ_mars_parallel</code>	Mars orbit and atmosphere	G-approx.	yes
<code>cratersQ_mars_full</code>	Mars orbit and atmosphere	yes	no

The current implementations use the following naming convention. The input topography to `horizons.f90` is `name.xyz`, and the output will be `horizons.dat` for the sequential implementation or `horizon.arg` for the parallel implementation, where `arg` is an integer.

`cratersQ_*` expects input files `name.xyz`, `horizons.name`, and optionally `viewfactors.name`. File names and their associated parameters are specified in module `filemanager`, that the user edits.

The model also includes 1D subsurface heat conduction, eq. (1.1). Subsurface temperatures need to be equilibrated, and hence the entire model needs to be run much longer than would be necessary without subsurface heat. Lateral subsurface heat conduction is neglected. Without subsurface conduction, equilibrium temperatures, according to eq. (5.10) with $k = 0$, can be used, and in this case only a few steps of equilibration are needed to account for several orders of reflection.

`insol3d_earth` was used in Schorghofer et al. (2017) and Schorghofer (2018), `cratersQ_mars_parallel` in Schorghofer et al. (2019), `cratersQ_moon` in Hayne et al. (2021), and `cratersQ_mars_full` in Schorghofer (2020).

Bibliography

- Aharonson, O. and Schorghofer, N., 2006. Subsurface ice on Mars with rough topography. *J. Geophys. Res.* 111(E11):E11007. doi: 10.1029/2005JE002636.
- Dozier, J. and Frew, J., 1990. Rapid calculation of terrain parameters for radiation modeling from digital elevation data. *IEEE Transactions on Geoscience and Remote Sensing* 28(5): 963–969. doi: 10.1109/36.58986.
- Flo Heggem, E. S., Etzelmüller, B., and Berthling, I., 2001. Topographic radiation balance models: sensitivity and application in periglacial geomorphology. *Norsk Geografisk Tidsskrift-Norwegian Journal of Geography* 55(4):203–211. doi: 10.1080/00291950152746531.
- Hayne, P. O., Aharonson, O., and Schorghofer, N., 2021. Micro cold traps on the Moon. *Nature Astronomy* 5:169–175. doi: 10.1038/s41550-020-1198-9.
- Kreslavsky, M. A. and Head, J. W., 2005. Mars at very low obliquity: atmospheric collapse and the fate of volatiles. *Geophys. Res. Lett.* 32(12):L12202. doi: 10.1029/2005GL022645.
- Rakovec, J. and Zakšek, K., 2012. On the proper analytical expression for the sky-view factor and the diffuse irradiation of a slope for an isotropic sky. *Renewable Energy* 37(1): 440–444. doi: 10.1016/j.renene.2011.06.042.
- Schorghofer, N., 2018. Permafrost survey on the Maunakea summit plateau: Final report. Technical report, University of Hawaii. 28pp.
- Schorghofer, N., 2020. Mars: Quantitative evaluation of crocus melting behind boulders. *Astrophys. J.* 890:49. doi: 10.3847/1538-4357/ab612f.
- Schorghofer, N. and Edgett, K. S., 2006. Seasonal surface frost at low latitudes on Mars. *Icarus* 180(2):321–334. doi: 10.1016/j.icarus.2005.08.022.
- Schorghofer, N., Leopold, M., and Yoshikawa, K., 2017. State of high-altitude permafrost on tropical Maunakea volcano, Hawaii. *Permafrost and Periglacial Processes* 28:685–697. doi: 10.1002/ppp.1954.

- Schorghofer, N., Levy, J. S., and Goudge, T. A., 2019. High-resolution thermal environment of recurring slope lineae in Palikir Crater, Mars, and its implications for volatiles. *J. Geophys. Res.* 124:2852–2862. doi: 10.1029/2019JE006083.
- Spiga, A. and Forget, F., 2008. Fast and accurate estimation of solar irradiance on martian slopes. *Geophys. Res. Lett.* 35:L15201. doi: 10.1029/2008GL034956.

Part 6

Surface-bounded Exospheres

Monte-Carlo Model of Ballistically Hopping Molecules in Gravitationally-Bound Exospheres

History: developed 2012–2017

Core routines are implemented in `montecarlo.f90`

6.1 Introduction

The ballistic trajectories of neutral molecules or atoms in a surface-bounded exosphere are simulated with a Monte-Carlo method. Individual water molecules are launched with probabilistically distributed cartesian velocity components that amount to a random initial azimuth and thermal speed appropriate for the local surface temperature. The model then computes the molecule's impact location and time analytically. An event-driven algorithm is used, where landing and launching events are processed in time-order. Events are scheduled and processed until the molecule is destroyed or lost or until its landing or launch time is beyond the next thermal model time step, when surface temperatures are updated.

Each molecule has a longitude $\mathbf{p}_r[1]$, latitude $\mathbf{p}_r[2]$, status \mathbf{p}_s (on surface =0, in-flight =1, lost or cold-trapped < 0), and time to the next event \mathbf{p}_t (until it arrives on the surface or until it will leave the surface). Negative status values can be used to keep track of where the particle is trapped or how it was lost. Surface temperatures are calculated with a 1D thermal model, as in Part 1.

6.2 Ballistic Flight on Sphere

d ... flight distance (measured along surface of sphere)

t ... duration of flight

τ_{res} ... surface residence time

τ_{dissoc} ... photo-destruction time scale

v_{esc} ... escape speed

v_1 ... initial velocity along longitude direction

v_2 ... initial velocity along meridian

v_3 ... initial vertical (radial) velocity component

az ... azimuth

$\Delta\phi$... difference in longitude

λ ... latitude

M ... molar mass

R_{moon} ... radius of body

A ballistic molecule moves on a plane that goes through the center of sphere/body; the ground track is thus part of a great circle.

6.2.1 Constant gravity

For constant g ,

$$t = 2v_3/g \quad (6.1)$$

$$d = \frac{2}{g}v_3\sqrt{v_1^2 + v_2^2} \quad (6.2)$$

If $|v| > 0.4v_{\text{esc}}$, then use non-uniform gravity formulae (Sec. 6.2.2)

If $|v| > v_{\text{esc}}$, then gravitational escape

The landing latitude and longitude (λ_2 , $\phi_1 + \Delta\phi$) are calculated from the starting coordinates (λ_1 , ϕ_1) with the following equations:

$$\cos(az) = v_2/\sqrt{v_1^2 + v_2^2} \quad (6.3)$$

$$\sin \lambda_2 = \sin(d/R_{\text{moon}}) \cos(\lambda_1) \cos(az) + \sin(\lambda_1) \cos(d/R_{\text{moon}}) \quad (6.4)$$

$$\cos \lambda_2 = \sqrt{1 - \sin^2 \lambda_2} \quad (6.5)$$

$$\cos(\Delta\phi) = \frac{\cos(d/R_{\text{moon}}) \cos(\lambda_1) - \sin(\lambda_1) \sin(d/R_{\text{moon}}) \cos(az)}{\cos \lambda_2} \quad (6.6)$$

Roundoff issues: if $\cos(\Delta\phi) > +1$ then $\cos(\Delta\phi) = +1$; if $\cos(\Delta\phi) < -1$ then $\cos(\Delta\phi) = -1$.

$$p_r(2) = \arcsin(\sin \lambda_2)$$

$$\Delta\phi = \arccos(\cos(\Delta\phi)) \text{ for normalization}$$

if $v_1 < 0$, then $\Delta\phi = -\Delta\phi$

$$p_r(1) = p_r(1) + \Delta\phi$$

if $(\cos \lambda_2 == 0)$ then on pole

$p_r(1)$ is normalized to 0...360°.

$$p_t = p_t + t$$

6.2.2 Non-uniform gravity

Ballistic travel distance d and flight duration t can also be calculated analytically for a radially dependent gravitational acceleration. Radial variations in g are small for typical thermal speeds on Mercury and on the Moon, but necessary for Ceres and for super-thermal species on the Moon. The following equations are derived from those in Vogel (1966) and Kegerreis et al. (2017).

a ... semi-major axis of ballistic trajectory

e ... eccentricity of ballistic trajectory

α ... zenith angle of launch velocity, $\alpha = \arctan\left(\sqrt{v_1^2 + v_2^2}/v_3\right)$

Instead of (6.1) and (6.2) use

$$\gamma = (|v|/v_{\text{esc}})^2 \quad (6.7)$$

$$a = \frac{R_{\text{moon}}}{2(1 - \gamma)} \quad (6.8)$$

$$e = \sqrt{1 - 4\gamma(1 - \gamma) \sin^2 \alpha} \quad (6.9)$$

$$d = 2R_{\text{moon}} \arccos\left(\frac{1}{e}(1 - 2\gamma \sin^2 \alpha)\right) \quad (6.10)$$

$$E_p = 2 \arctan\left(\sqrt{\frac{1+e}{1-e}} \tan \frac{d}{4R_{\text{moon}}}\right) \quad (6.11)$$

$$t = \frac{R_{\text{moon}}}{v_{\text{esc}}} \frac{E_p + e \sin E_p}{(1 - \gamma)^{3/2}} \quad (6.12)$$

These equations are not suitable for small launch velocities due to roundoff.

Round-off issues:

a) If e is very close to 1 (fast near-horizontal launch), then based on Taylor expansion of (6.10) and (6.11),

$$d = 4\gamma R_{\text{moon}} \sin \alpha \quad (6.13)$$

$$E_p = 2 \arctan \sqrt{\frac{\gamma}{1 - \gamma}} \quad (6.14)$$

b) If $1 - 2\gamma \sin^2 \alpha > e$ (horizontal launch), do something, otherwise $d = \text{NaN}$

Then use (6.3)–(6.6) as before.

6.2.3 Coriolis effect

The Coriolis effect is incorporated by adding tangential velocities but subtracting the distance the surface has traveled during time of flight.

At launch:

$$v_1 = v_1 - \frac{2\pi R_{\text{moon}}}{\text{siderealDay}} \cos(p_r(2)) \quad (6.15)$$

After landing:

$$p_r(1) = p_r(1) + t/\text{siderealDay} \quad (6.16)$$

The Coriolis effect is negligible on the Moon and on Mercury, but noticeable on Ceres.

	M	τ_{dissoc} (s)	
H ₂ O	18.015	20×3600	Potter and del Duca (1964)
H ₂ O		1/12.6e-6	Crovisier (1989), normal sun
H ₂ O		1/23.0e-6	Crovisier (1989), active sun
He	4.0026	1.9e7	Killen and Ip (1999)
Ar-40	39.96	3.2e6	Killen and Ip (1999)

Table 6.1: Some pertinent parameters. τ_{dissoc} = photodissociation time scale at 1 AU

6.3 Other Model Components

6.3.1 Initial velocities

At launch, each of the three velocity components is picked from a probability distribution. For a Maxwellian distribution, each velocity component is picked from a Gaussian distribution with standard deviation $\sqrt{T_{\text{surf}} 8314.5/M}$. This also results in uniformly distributed launch azimuths. Other probability distributions can be implemented, if desired. An Armand (also known as Maxwell-Boltzmann-Flux) distribution is provided as an option in the code.

6.3.2 Photo-destruction

Molecules are lost in-flight by photo-destruction (Table 6.1), at a rate of $t/(\tau_{\text{dissoc}} R^2)$, where R is the distance from the sun, often approximated by the semi-major axis. Requires incident flux $Q > 0$, since this only occurs on the dayside. A comprehensive compilation of photo-destruction rates can be found in Huebner et al. (1992). A database is maintained at <http://phidrates.space.swri.edu/>.

6.3.3 Event driver

Process events over the time step of the thermal model Δt_T , e.g., one hour

```

if ( $p_t > \Delta t_T$ ) exit
case( $p_s < 0$ ) exit ! not alive
case( $p_s == 0$ ) ! leaving
    hop once, update  $p_t$ 
case( $p_s == 1$ ) ! landing
    if (incoldtrap) then
         $p_t = \infty$ 
        cycle
    endif
    evaluate  $\tau_{\text{res}}(T_{\text{surf}})$ 
     $p_t = p_t + \tau_{\text{res}}$ 

```

After all events within Δt_T are processed, subtract Δt_T from all times: if ($p_s \geq 0$) $p_t = p_t - \Delta t_T$. (Moving time zero helps avoid truncation errors after a long run.)

6.3.4 Residence times

Temperature also sets the residence time of water molecules on the surface, which is negligible on most of the lunar dayside and very long on most of the lunar nightside. Many older models use a binary choice, where molecules either immediately hop on the day side or reside indefinitely on the surface on the nightside. This model uses a molecular residence time that depends continuously on temperature instead of a threshold temperature.

For crystalline ice, the average molecular surface residence time only depends on temperature T , but for adsorbed water it is also a function of the adsorbate density θ (number of H_2O molecules per area). The average residence time is given by

$$\tau_{\text{res}} = \frac{\theta_m}{E(T, \theta)} \quad (6.17)$$

where E is the sublimation rate and $\theta_m = 10^{19} \text{ m}^{-2}$ is the areal number density of an H_2O monolayer. A special case of this parametrization is $\tau_{\text{res}} = c\theta_m/E(T)$, where E is the sublimation rate of pure ice. For pure ice $c = 1$. For example, $c = 1/400$ is reasonable for 0.1 monolayers (Schorghofer and Aharonson, 2014). The functional form of $E(T)$ is almost the same as using a vibrational frequency multiplied by a Boltzmann (Arrhenius) factor.

For non-condensable exospheric species, e.g., helium, $\tau_{\text{res}} = 0$.

Discussion: A fraction of particles bounces elastically from the surface rather than accommodating thermally and leaving at a velocity unrelated to the incoming velocity. The fraction is closely related to the “accommodation coefficient” or “condensation coefficient”, and it is temperature dependent. The equilibrium vapor pressure is defined as the flux of water molecules from the gas to the condensed phase being equal to the flux in the opposite direction. Elastic (non-condensing) bounces are not directly implemented in the model.

The exosphere model was used in Schorghofer (2014) (with constant g) and Schorghofer et al. (2016, 2017a,b) (with non-uniform gravity).

Bibliography

- Crovisier, J., 1989. The photodissociation of water in cometary atmospheres. *Astron. Astrophys.* 213:459–464.
- Huebner, W. F., Keady, J. J., and Lyon, S. P., 1992. Solar photo rates for planetary atmospheres and atmospheric pollutants. *Astrophysics and Space Science* 195:1–294. doi: 10.1007/978-94-017-3023-5_1.
- Kegerreis, J. A., Eke, V. R., Massey, R. J., Beaumont, S. K., Elphic, R. C., and Teodoro, L. F., 2017. Evidence for a localized source of the argon in the lunar exosphere. *J. Geophys. Res.* 122:2163–2181. doi: 10.1002/2017JE005352.
- Killen, R. M. and Ip, W.-H., 1999. The surface-bounded atmospheres of Mercury and the Moon. *Reviews of Geophysics* 37:361–406. doi: 10.1029/1999RG900001.

- Potter, A. E. and del Duca, B., 1964. Lifetime in space of possible parent molecules of cometary radicals. *Icarus* 3:103. doi: 10.1016/0019-1035(64)90051-X.
- Schorghofer, N., 2014. Migration calculations for water in the exosphere of the Moon: Dusk-dawn asymmetry, heterogeneous trapping, and D/H fractionation. *Geophys. Res. Lett.* 41: 4888–4893. doi: 10.1002/2014GL060820.
- Schorghofer, N. and Aharonson, O., 2014. The lunar thermal ice pump. *Astrophys. J.* 788: 169. doi: 10.1088/0004-637X/788/2/169.
- Schorghofer, N., Mazarico, E., Platz, T., Preusker, F., Schröder, S., Raymond, C., and Russell, C., 2016. The permanently shadowed regions of dwarf planet Ceres. *Geophys. Res. Lett.* 43:6783–6789. doi: 10.1002/2016GL069368.
- Schorghofer, N., Byrne, S., Landis, M. E., Mazarico, E., Prettyman, T. H., Schmidt, B. E., Villarreal, M. N., Castillo-Rogez, J., Raymond, C. A., and Russell, C. T., 2017a. The putative cerean exosphere. *Astrophys. J.* 850:85. doi: 10.3847/1538-4357/aa932f.
- Schorghofer, N., Lucey, P., and Williams, J.-P., 2017b. Theoretical time variability of mobile water on the moon and its geographic pattern. *Icarus* 298:111–116. doi: 10.1016/j.icarus.2017.01.029.
- Vogel, U., 1966. Molecular fluxes in the lunar atmosphere. *Planetary and Space Science* 14: 1233–1252. doi: 10.1016/0032-0633(66)90078-X.